Subsurface Characterization of the Coso Geothermal Field and Surroundings by Ambient Noise Tomography

Yingjie Yang, Michael H. Ritzwoller, and Craig H. Jones
University of Colorado at Boulder, Boulder, CO 80309-0390 (yingjie.yang@colorado.edu)

Abstract: We apply seismic ambient noise tomography to image and investigate the shallow shear velocity structure beneath the Coso Geothermal Field and surrounding areas. Data from a PASSCAL experiment operated within the Coso Geothermal region between 1998 and 2000 and surrounding broadband stations from the Southern California Seismic Network (SCSN) are acquired and processed. Daily cross-correlations of ambient noise between all pairs of stations that overlapped in time of deployment were calculated and then stacked over the duration of deployment. Phase velocities of Rayleigh waves between 3 to 10 sec period are measured from the resulting cross-correlations. Depending on period, between about 300 to 600 reliable phase velocity measurements are inverted for phase velocity maps from 3 to 10 sec period, which in turn are inverted for a 3D shear velocity model beneath the region. The resulting 3D model reveals features throughout the region that correlate with surface geology. Beneath the Coso Geothermal Area shear velocities are generally depressed, a prominent low velocity anomaly is resolved clearly within the top 2 km, no significant anomaly is seen below about 14 km depth, and a weakly resolved anomaly is observed between 6 and 12 km depth. The anomaly in the top 2 km probably results from geothermal alteration in the shallow subsurface, no magmatic body is imaged beneath 14 km depth, but the shear velocity anomaly between 6 and 12 km may be attributable to partial melt. The thickness and amplitude of the magma body trade-off in the inversion and are ill-determined. Low velocities in the regions surrounding Coso at depths near 7 km underlie areas with Miocene to recent volcanism, suggesting that some magmatic processing of the crust could be focused near this depth.

Submitted to *Geochemistry, Geophysics, and Geosystems*, September 2010.

1. Introduction

The Coso Geothermal Area lies at the southwestern corner of the actively deforming part of the Basin and Range and within the Eastern California Shear Zone. This region is unusual in apparently accommodating westward motion of the Sierra Nevada through a complex combination of surficial normal, thrust, and strike-slip faulting as well as vertical-axis rotation (e.g.,Jones, 1987; Hauksson and Unruh, 2007; Taylor et al., 2008; Pluhar et al., 2006). It also lies in the last part of the Basin and Range to experience significant volcanism (e.g., Armstrong and Ward, 1991; McQuarrie and Oskin, in press). The Coso Range contains one of the young magmatic centers along the western margin of the Basin and Range that originated about 4 Ma but entered a phase of bimodal volcanism about 1 Ma (Duffield et al., 1980). Among the more intriguing suggestions has been that the Coso Geothermal Area overlies an emerging core complex representing rising lower crustal rock with an associated magmatic system (Monastero et al., 2005).

An exceptionally diverse collection of geophysical and geological analyses have been applied to the Coso Geothermal Area and surroundings, largely in an attempt to characterize the geothermal resource being exploited for the generation of electricity. Much of the work characterizes the uppermost few kilometers of the crust, including active source refraction and reflection profiling (Pullammanappalil et al., 2001; Unruh et al., 2008), local earthquake source characteristics (Feng and Lees, 1998; Hough et al., 1999; Bhattacharyya et al., 1999, 2002; Hauksson and Unruh, 2007), seismic velocity tomography from local earthquakes (Walck and Clayton, 1987; Walck, 1988; Wu and Lees, 1999; Lees and Wu, 2000; Hauksson and Unruh, 2007), magnetotellurics (Newman et al., 2008), seismic attenuation tomography (Young and Ward, 1980, Sanders et al., 1988; Wu and Lees, 1996, Hough et al., 1999), and surface heat flow (Combs, 1980). The overall picture of the region from these works is of a complex brittlely deforming crust above ~4 km depth in the vicinity of the geothermal area, with brittle failure extending to 8-12 km depth in the surrounding area.

Deeper variations in structure have been probed less frequently, in part because of the complications near the surface, in part because of the absence of deeper local seismicity, and in part because of the focus on shallow structure relevant to geothermal exploration. Within the Coso Geothermal Area, two main questions have emerged: the depth of the magma chamber(s) acting as the heat source and the relationship of magmatism to faulting or shearing at depth. Three main studies bear on the structure of the Coso geothermal field below 5 km depth: a teleseismic receiver function study by Wilson et al. (2003), a regional and local earthquake travel time tomography study by Hauksson and Unruh (2007) and an active source reflection profile by Unruh et al. (2008). Both the receiver function and reflection profile experiments observe a strong seismic converter/reflector at about 5 km depth. Wilson et al. (2003) interpreted this as the top of the magma chamber containing at least 1.5% melt, an interpretation consistent with a petrological analysis by Manley and Bacon (2000). Hauksson and Unruh (2007), in contrast, infer from Vp/Vs ratios that the volume between about 5 and 10 km depth cannot contain melt. In their interpretation, the magma chamber is below ~10 km, under a deeper reflector seen by Unruh et al. (2008). Hauksson and Unruh (2007) suggest that the discrepancy with Wilson et al. (2003) resulted from the limited vertical resolution of vertical rays. Receiver functions, however, do provide good vertical resolution but are insensitive to small gradients in wave speeds. An alternative explanation for the discrepancy is the lack of horizontal resolution in the local earthquake tomography both because of the absence of local earthquakes within or beneath the purported magma chamber and because of raybending around extreme low-velocity bodies. In any event, the depth of any magma chamber and the ultimate source of the heat for the geothermal field remains disputed.

In the past few years, novel interferometric methods of seismic imaging based on ambient noise have been developed. Methods based on ambient noise, called “ambient noise tomography” (ANT), have proven effective (Shapiro et al., 2005; Sabra et al., 2005) at extracting short period (6 – 30 sec) surface waves from ambient seismic noise to constrain structures in the middle to lower crust and the uppermost mantle. Ambient noise tomography is based on cross-correlations

of long recordings of seismic noise observed between pairs of stations to construct surface wave dispersion measurements at short and intermediate periods. Previous studies based on ambient noise tomography have been applied mostly at regional scales including in New Zealand (Lin et al. 2007), Southern Africa (Yang et al. 2008a), Spain (Villaseñor et al. 2007), Korea (Cho et al. 2007), Japan (Nishida et al. 2008), Tibet (e.g., Yao et al., 2006), and the western US (Moschetti et al. 2007, 2010b; Lin et al. 2008; Yang et al. 2008b; Lin et al., 2010) but also at continental scales across Europe (Yang et al. 2007), China (Zheng et al., 2008; Yang et al., 2010), the USA (Bensen et al. 2008, 2009), and Australia (Saygin and Kennett 2010).

In this study, we apply ambient noise tomography at a sub-regional scale with an aperture of ~200 km to image shallow Vs structures beneath the Coso Geothermal Area and surrounding areas. The purpose is to attempt to constrain the depth of any magma chambers underlying the area using ambient noise dispersion measurements. To improve resolution of the shallow crust ambient noise dispersion measurements are extended down to 3 sec period. The relatively narrow aperture of the study, however, prohibits extending measurements above about 10 sec period.

2. Data and methods

Twenty sub-arrays of the Coso PASSCAL experiment were deployed in and near the Coso Geothermal Area from November 1998 to May 2000 (e.g., Wilson et al., 2003). Each array consisted of 5–8 short-period, three-component sensors (Mark Products L22 or L4c, and/or Teledyne Geotech S-13) spaced ~500 m apart and arranged into two orthogonal lines with, when available, 1–3 broadband sensors (Guralp CMG3-ESP, CMG-40T). These 20 sub-arrays had numerous overlaps in time of deployment, which results in many interstation ray paths between coeval subarrays. Overall, about 143 station sites were occupied in this experiment. Surrounding this PASSCAL experiment, there are about 67 seismic stations from the Southern California Seismic Network (SCSN), 30 equipped with broadband sensors and the rest equipped with short-period sensors. Continuous data since 1998 from 20 of these SCSN stations are archived at the IRIS/DMC, which allows us to obtain cross-correlations between the stations of the Coso

PASSCAL experiment and the SCSN stations. Data recorded after January, 2008 from the rest of the 67 SCSN seismic stations were acquired from the online data center at the Southern California Earthquake Center (SCEC). The locations of these stations are plotted in Figure 1.

Even though some stations used in this study possess short-period sensors with a pass-band above 1 Hz, significant ambient noise energy can still be observed in the period range from 1 to 10 sec. Figure 2 shows the spectra of ambient seismic noise recorded at several short-period (stations LBE1, LBTE5 and WHAE1) and broadband stations (stations MPM and WHA00). These spectra are quite similar between 0.1 and 1 Hz (1 to 10 sec period) for both short-period and broadband stations. The largest amplitudes are in the microseismic band between 0.1 and 0.2 Hz (5-10 sec). Spectra decay gradually away from the microseismic band and tend to be nearly flat at frequencies higher than 0.2 Hz (periods <5 sec). As demonstrated in section 3, surface waves at periods from 3 to 10 sec can be extracted from cross-correlations among the short-period stations, between short-period stations and broadband stations, or among the broadband stations (Fig.5).

After accumulating continuous seismic data, we first check for possible errors in timing and polarization based on the first arrivals of earthquake waves (P-waves). We find that several PASSCAL stations have timing errors, although no timing errors are found for the SCSN stations. The PASCCAL stations with timing errors are removed from the data set because there are nearby stations within each sub-array. We also find that some short-period PASSCAL stations have reversed vertical polarities compared to broadband stations. Before further data processing, we reverse the vertical time series of those stations to align them with the vertical polarity of the broadband stations.

Most (but not all) short-period stations from the Coso PASSCAL network have glitches in the time domain while broadband stations are glitch-free. These glitches were typically generated by difficulties with the electronics of a preamplifier used to expand the frequency response of many of the instruments. Examples of seismograms with glitches and without glitches are plotted in

Figure 3a. The amplitude, width and time interval of the glitches vary between stations. However, these glitches are typically at low frequencies, with large amplitudes mainly at periods between 50 and 100 sec. After we apply a high-pass filter to the seismograms with a corner frequency at 0.1 Hz, glitches become much smaller (Figure 3b). To remove the effect of glitches more completely, we further apply a running-absolute-mean normalization. This normalization computes the running average of the absolute value of the waveform in a normalization time window of fixed length and weights the waveform at the centre of the window by the inverse of this average. The width of the normalization we use here is 1 sec. The running-absolute-mean normalization suppresses the amplitude of glitches to the same level as the ambient noise (Figure 3c).

The data processing procedure applied here is very similar to that described in detail by Bensen *et al*. (2007, 2008) and Lin et al. (2008). Using only the vertical component of ambient noise implies that the cross-correlations we obtain predominantly contain Rayleigh wave signals. Continuous data are decimated to ten samples per second and then filtered in the period band from 1 to 10 sec. Instrument responses are removed from the continuous data because different types of seismic sensors are used among the stations. Because the amplitudes of ambient noise at ~6 sec period dominate the spectra (Fig. 2), spectral whitening is applied to flatten spectra over the entire period band (1-10 sec). Time-domain normalization then is applied to suppress the influence of earthquake signals and other irregularities, such as the glitches observed in the seismograms from some Coso PASSCAL stations (Fig.3). After these processes are completed, cross-correlations are performed daily in the period band from 1-10 sec and then are stacked over the fifteen-month period between March 1999 and May 2000 for the Coso PASSCAL stations and the 20 SCSN stations. Over the twenty-one month period from January 2008 to September 2009, cross-correlations are performed similarly between the 67 SCSN stations.

3. Results of cross-correlations

In this study, we aim to retrieve surface waves at periods from 1 to 10 sec, which would provide good constraints on Vs from the surface to ~20 km depth. However, as discussed in section 2, spectra of ambient noise have large amplitudes in the microseismic band between 0.1 and 0.2 Hz (5-10 sec) but decay rapidly at frequencies higher than 0.2 Hz (<5 sec) (Fig. 2). As a result, the shortest period of surface waves extracted from cross-correlations of ambient noise is 3 sec. Figure 4 shows examples of one-month cross-correlations among the Coso PASSCAL stations filtered in two period bands: 1-3 sec and 3-10 sec. There are strong and coherent surface wave signals in the cross-correlations at 3-10 sec periods, but,at 1-3 sec period there are no clearly aligned surface wave signals and the cross-correlations are much noisier. In a separate unpublished study, Yang and Ritzwoller (Spectral characteristics of ambient seismic noise and coda waves at periods from 1-10 sec, in preparation) showed that ambient noise between 1 and 3 sec period dominantly arises from the Pacific coast in the westernmost US and these waves are strongly attenuated are they propagate inland. Consequently, in the Coso area the amplitude of ambient noise at 1-3 sec period is very low, which results in very weak surface wave signals in the cross-correlations. In the cross-correlation analysis here, we focus on the period band from 3-10 sec, which allows us, ultimately, to constrain shear velocities in the subsurface from the surface to ~15-20 km depth.

Figure 5 shows the cross-correlations filtered at 3-10 sec period between a broadband station CLC and other distant stations from the Southern California Seismic Network (SCSN) as well as between a short-period station WRC and other SCSN stations. The locations of the stations CLC and WRC situated near the Coso Geothermal Area are shown in Figure 1a. Surface wave signals appear at either positive or negative correlation lag times with an average move-out speed of ~3 km/sec, as delineated by the inclined dashed lines. The waveforms of cross-correlations between short-period stations or broadband stations are very similar between 3 and 10 sec period. To simplify data analysis and enhance the SNR, we separate each cross-correlation into positive and

negative lag components and then add the two components to form a final cross-correlation, called the "symmetric component". The following analyses are performed exclusively on symmetric components.

4. Dispersion measurements and data selection

Bensen et al. (2007) showed that uncertainties of group velocity dispersion measurements from cross-correlations are much larger than those of phase velocity measurements. Thus, we only construct phase velocity dispersion maps between 3 and 10 sec period and then use these maps to invert for a 3D shear wave velocity model of the subsurface. Phase velocity dispersion measurements of Rayleigh waves are obtained from the symmetric components of inter-station cross-correlations by automatic frequency-time analysis (FTAN) (e.g., Bensen et al., 2007).

Figure 6 shows two examples of measured phase velocity dispersion curves. The path between stations CGO and LRL (red line) passes through the Coso Geothermal Area, while the path between stations CWC and TEH (blue line) passes through the Sierra Nevada. Phase velocities of the CGO-LRL path (red line) are significantly lower than those of the CWC-TEH path, which indicates generally lower seismic velocities in the Coso Geothermal Area and higher velocities in the Sierra Nevada.

The automated FTAN dispersion measurements are winnowed by applying three criteria to select reliable measurements for surface wave tomography. First, the distance between two stations must be greater than three wavelengths to ensure that full surface wave packets can be separated from precursory noise and interpreted as far-field measurements (Tsai and Moschetti, 2010). Second, the signal-to-noise ratio (SNR) must be higher than 15 at an individual period for the measurement at that period to be accepted. SNR is defined as the ratio of the peak amplitude within a time window containing the surface wave signal to the root-mean-square of the noise trailing the signal arrival window. Third, we require that the measurements agree with one another across the data set. This condition is tested during tomography as discussed in the next

section. Measurements that can be fit well by a smoothed tomographic map are considered to cohere with the data set as a whole.

Our data selection criteria result in a maximum of 590 measurements at 6 sec period being chosen for tomography from the ~6000 original inter-station velocity measurements. The numbers of selected paths as a function of period are listed in Table 1. The final number declines at smaller periods, so that there are only about 310 measurements chosen for tomography at 3 sec period because ambient noise at periods shorter than 5 sec is very weak. The number also reduces above 6 sec period, mainly due because of the three-wavelength criterion for inter-station distances.

We compute uncertainties for the dispersion measurements based on repeating cross-correlations over different time spans, as Yang et al. (2007) did using individual three-month cross-correlations. Because the installation durations of individual sub-arrays of the Coso PASSCAL experiment vary from one to three months, time-series lengths of stacked cross-correlations range from one month to three months. Given the short time lengths of cross-correlations, it is inappropriate to perform uncertainty analysis of measurements from the Coso PASSCAL stations. Thus, we only estimate measurement uncertainties for cross-correlations between SCSN stations. The average uncertainties of phase velocity measurements between the SCSN stations are about 20 m/s to 30 m/s with slightly higher uncertainties at longer periods, about 0.7-1.0% of the measured phase velocity values.

5. Surface wave tomography and construction of a 3D shear velocity model

We perform surface wave tomography on the selected dispersion measurements to produce Rayleigh wave phase velocity maps on a 0.25° by 0.25° grid using the method of Barmin et al. (2002). This tomography is performed in two steps. In the first, preliminary, step, an overly smoothed map is generated at each period in order to identify and reject bad measurements. This composes the third selection criterion discussed in section 4. We discard phase velocity

measurements with travel time residuals larger than 2 sec. The second step of tomography is the construction of the final phase velocity maps that are laterally smoothed less than the maps constructed in the first step. The tomography method also provides corresponding resolution information, which is summarized by fitting a 2-D symmetric spatial Gaussian function to the resolution surface at each node: $A\exp\left(-\frac{|r|^2}{2\gamma^2}\right)$ (Levshin et al., 2005). The spatial resolution at each node is defined as twice the standard deviation of this Gaussian function: γ. Examples of resolution maps and associated path coverage at 4 and 9 sec period are plotted in Figure 7. Resolution is estimated to be about 40 km in most areas of the study region,but degrades towards the fringes.

The resulting phase velocity maps at 3, 5, 7 and 9 sec period are shown in Figure 8. Velocity perturbations are only plotted in the areas encompassing stations as outlined by the pentagons. The most pronounced features are high Rayleigh wave velocities along the Sierra Nevada and low velocities in the Basin and Range province to the east of the Sierra Nevada, especially near the Coso Geothermal Area. We do not discuss the observed variations of the phase velocity maps in detail because they are inverted for a 3D Vs model, which we discuss later in the paper.

Example local dispersion curves for a point in the Sierra Nevada and at the Coso Geothermal Area (Fig. 9a) extracted from the phase velocity maps from 3 to 10 sec period are shown in Figure 9b. These and similar curves elsewhere are inverted for Vs profiles beneath all grid points. Vertical Vs profiles beneath these two locations are shown in Figure 9c. The model is strongly damped vertically to ensure that vertical differences between nearby layers are minimal. The 3D Vs model then is constructed by assembling all of the Vs profiles. Because the longest period of the Rayleigh waves in the inversion is 10 sec, which has a peak sensitivity at around 10 km depth and fair sensitivity up to ~20 km, the deepest structure we can resolve is between 15 and 20 km.

To construct the Vs model we perform a linearized inversion of each Rayleigh wave phase speed

curve for the best fitting Vs model below each grid point. In the linearized inversion, depth-dependent shear wave speeds are parameterized in eight layers from the surface to a depth of 20 km with the thickness varying from 2 km at the surface to 5 km at 20 km depth. Partial derivatives of phase velocity at each period relative to Vs at various depths are calculated using the method of Saito DISPER80 (Saito, 1988). During the inversion, adjacent layers of the Vs model are smoothed vertically between neighboring layers in order to reduce the likelihood of vertical oscillations in the model. At most places a vertically smooth model can fit the data quite well, but in section 6 we discuss further the effect of weakening this constraint in the Coso area. Because Rayleigh wave phase speeds depend primarily on Vs, we scale Vp to Vs using a constant Vp/Vs ratio of ~1.73, which approximately is the average Vp/Vs ratio found by Hauksson and Unruh (2007). We take the one-dimensional average model of Hauksson (2000) as the starting model in our model.

Although we estimated uncertainties in most of the dispersion measurements, we do not have estimates of uncertainties in the shear-wave velocity structure. However, misfit to the measurements from the 3D model is approximately constant with period and averages between 40 m/s and 50 m/s, which is a fairly good estimate of the uncertainty in the local dispersion curves, such as those shown in Figure 9b.

6. Discussion

Figure 10 shows the maps of shear velocity at depths of 1, 3, 6, 10, 14 and 18 km plotted as perturbations relative to the average values across the maps at each depth. The most pronounced high velocity is observed beneath the Sierra Nevada, which is composed primarily of Mesozoic granitic plutons and is probably colder and less faulted than other regions in this study area (e.g., Saltus and Lachenbruch, 1991; Combs, 1980). The eastern margin of this high velocity anomaly follows the eastern front of the Sierra Nevada in the top 6 km but gradually retreats towards the west at greater depths. This westward retreat with depth suggests that Sierran crust is being

modified from below, either thermally (e.g., Saltus and Lachenbrush, 1991) or mechanically by west-dipping low-angle normal faults (e.g., Wernicke, 1985; Jones, 1987; Jones and Phinney, 1998). Within the southern Sierra Nevada, low velocities are imaged in the top 3 km of the crust near Lake Isabella, which may be due to the presence of sediments or deformation associated with the proto-Kern Canyon or Kern Canyon fault zones. In the upper crust (<10 km), prominent low velocities are imaged beneath the Coso Geothermal Area, which are probably related to high temperatures and perhaps the presence of partial melt. The depth range of these low velocities is consistent with receiver function studies, such as Wilson et al. (2003). This is discussed further below. Another pronounced shallow low velocity is also imaged near 242° 15' just south of the Garlock Fault. Velocities in the uppermost 2 km and 6-10 km beneath northern Death Valley are also low. In the middle crust from 10 to 20 km, the most pronounced feature is the low velocities beneath the southern Great Valley, perhaps reflecting deeper sediments than expected, Miocene tectonism, or possibly Rand schist in the lower crust (e.g., Bartow, 1984).

In general, the 3D model of shear velocity structure (Fig. 10) displays anomalies that correlate with surficial geologic features, suggesting that the analysis has captured wave speed variations reflecting local geology. Most prominent are the high velocities beneath the Sierra Nevada, consistent with the relatively unfaulted plutonic framework of the range. Bedrock in the mountains north of the Garlock Fault also tend to have higher waves speeds than average in the top 5 km of the crust with the notable exception of the Coso Range and, perhaps, the southern Inyo Mountains. Sedimentary basins are less distinctly imaged. The Cantil Basin just south of the Garlock Fault near longitude 242.25° is a notable low velocity feature at ~1 km depth, consistent with both the substantial gravity low in the basin and seismic reflection imaging (e.g., Pullammanappallil and Louie, 1993). Death Valley is also a prominent shallow low, consistent with the accumulation of sediments in that basin (e.g., Blakely et al., 1999). Other prominent basins, such as Owens Lake and Indian Wells Valley, are not particularly evident in the inversion results. The absence of Indian Wells Valley in particular, given its presence in P-wave images of

Hauksson and Unruh (2007), suggests either an error in one analysis or the other or the presence of unusual valley fill with a very low Vp/Vs ratio.

An intriguing feature of this study are low velocities between about 6 and 8 km depth under much, but not all, of the Basin and Range (Fig. 10c, 11). This feature correlates well with the extent of sizeable exposures of Neogene and Quaternary volcanic rocks (**Fig. 11**), strongly suggesting a magmatic origin. Within the area well resolved by this study, only the older Miocene volcanic center in the southern Sierra and some small volume centers in the eastern Sierra remain outside this zone. It is implausible that this entire feature represents uniformly distributed melt at these depths, but local accumulations of melt seem consistent with very low resistivities found near these depths north of Coso (Park and Wernicke, 2003). This anomaly probably results from crust profoundly reworked by igneous processes over the past few million years. The modern low velocities may represent some combination of melt, alteration, magmatic fluids and high temperatures. We explore some aspects of this feature more thoroughly in the vicinity of the Coso volcanic field, where this feature is better sampled and where other work, summarized in the Introduction, provides some constraints on the nature of this anomaly.

Three vertical Vs transects are plotted as absolute and relative velocities in Figure 12, with the positions of these Vs transects indicated on the 1 km shear velocity map (Fig. 10a). Low velocities in the entire depth column beneath the Coso Range are quite close to the position of the Coso Geothermal Field. In particular, there is a very low velocity feature imaged in the top 2 km. The appearance of this anomaly, despite the dominant surface exposure of granite, suggests profound alteration of the crust in the area and/or significant influence from shallow magmatic or hydrothermal fluids. This feature, absent at equivalent depths from the local earthquake tomography of Hauksson and Unruh (2007), appears to underlie the northern part of the rhyolite domes of the Coso volcanic field and extend under the northern Coso Range. The area immediately south and east of the geothermal field has relatively high velocities.

Although the entire crustal column beneath the Coso Geothermal Area appears to have depressed Vs speeds (Figs. 9c, 12), there is an indication of a low velocity zone between depths of 6 and 8 km. This may reflect a deeper magmatic anomaly underlying the shallow geothermally induced anomaly in the top 2 km. The absence of profound low velocities below ~14 km (Figure 10e) tends to support a shallow magmatic interpretation. As noted above, these low velocities between 6 and 8 km depth extend over much of the region (e.g., beneath Death Valley, Fig. 12, A-A'), although several studies discussed low velocity zones beneath Death Valley (e.g., de Voogd, et al., 1986) and suggested a magmatic origin. Thus, it is important to test the resolvability of a shallow magmatic body (6-10 km) and the ability to separate such a body from anomalies above and below it.

As a first test to gain insight into vertical resolution, we consider dispersion curves for low velocity anomalies in depth ranges from 1-4 km (red), 6-10 km (pink), and 10-15 km (blue), respectively, as seen in Figure 13a. The amplitude of the velocity anomaly is 10% for the whole low velocity body. Rayleigh wave phase velocities from these models are presented in Figure 13b together with a background model. Inspection of the dispersion curves shows that to resolve anomalies at depths from 1-4 km from those at 6-10 km requires observations below 6 sec period, which we have. Resolving shallow and deep magmatic bodies at 6-10 km versus 10-15 km is harder, however. Measurements below 6 sec period are still needed, but the phase speed differences presented by these anomalies are smaller. In this case, with a 10% anomaly, differences are only about 50 m/s, which is approximately equal to the uncertainty in the phase speed maps.

Second, to test the vertical and lateral resolution we consider the ability to image three depth anomalies similar to those in the previous test, but with depth ranges that differ slightly from those in Figure 13. The initial model is laterally homogeneous and taken from the average of the inversion with real data except a low velocity anomaly is introduced beneath the COSO Geothermal Area. The lateral extent of this low velocity body is a 0.5° x 0.5° square centered at

117.875°, 36.125°N. We plot cross sections of the input Vs structures in Figure 14 (left column) along latitude 36.125°N From the three input models under each grid node, we first calculate the dispersion curves from 3 to 10 s period for Rayleigh wave phase velocities. Then, we construct phase velocity maps at the individual periods. At each period, we calculate the travel times and the average phase velocities between individual paths as in our real data. We also add Gaussian random noise with a 0.5 s standard deviation to the travel times of individual paths, similar to the standard deviation of the misfit in the tomography with real data. Using the calculated phase velocities of paths at different periods as the synthetic data, we perform the same inversion as described for the real data; that is, constructing phase velocity tomography maps, then extracting phase velocity dispersion curves at each grid from phase velocity maps, and finally inverting for shear wave velocities beneath each grid to construct a 3-D Vs model. Cross sections of the recovered Vs structure are plotted in Figure 14 (right column) for comparison with the input. The shape of a low velocity body between 0-6 km depth is recovered quite well, with limited vertical smearing. However, the deeper anomalies are smeared significantly vertically. The anomaly between 4-10 km is smeared at both top and bottom, but only at the bottom for the anomaly at 8-16 km. For all cases, the amplitude of the anomaly is damped by ~50%. The extent of amplitude damping would increase for thinner bodies.

As a final test, we reconsider the inversion of the dispersion data near the Coso Geothermal Area, shown in Figure 9b. In Figure 15, however, we reduce the strong vertical smoothing applied in the inversion across the entire area. We see that reducing smoothing results in amplifying the low velocity zone between depths of 8 and 12 km while increasing the velocities below at 15 km and below. Thus, although the strength of the low velocity zone between 6 and 12 km is not well constrained, a confined low velocity zone beneath 14 km is inconsistent with our data.

In conclusion, the resolution tests show that our data and methods are able to resolve a low velocity body situated in the top 5 km. Deeper anomalies are harder to resolve, but the absence of prominent low velocities beneath about 14 km depth in our estimated model (Fig. 10, 12)

beneath the Coso Geothermal Area is inconsistent with a deep seated magmatic source below this depth. The somewhat depressed low velocities observed between 6 and 8 km (Fig. 12, A-A') may reflect a magmatic body near this depth whose velocity anomaly is underestimated due to the intrinsic limitations in resolution in this depth range and the fact that we have strongly smoothed the model in the inversion. Applying somewhat less vertical smoothing further reduces Vs speeds between 8 and 12 km beneath the Coso Geothermal Area, as seen in Figure 15. This is consistent with the existence of a magmatic body within the depth range from 6 and 12 km beneath the Coso Geothermal Area. The causative body may be much thinner than this. It must be noted, however, that this interpretation is pushing the resolution limits of this study.

7. Summary and Conclusions

We processed continuous seismic data from a PASSCAL experiment that operated between 1998 and 2000 as well as surrounding broadband stations from the Southern California Seismic Network (SCSN). Daily cross-correlations were performed between all pairs of stations that overlapped in time of deployment and were then stacked over the deployed durations. Signal-to-Noise Ratio (SNR) and phase and group velocities of Rayleigh waves were measured with an automated FTAN procedure for each stacked cross-correlation. Then, three selection criteria determined the reliable measurements for surface wave tomography, which numbered between 288 and 590 paths across the study region, depending on period.

We inverted all of the phase velocity measurements for phase velocity maps between periods of 3 and 10 sec and the resulting phase velocity maps for a 3D shear velocity model by a strongly vertically smoothed linearized inversion. This 3D model reveals generally depressed shear velocities beneath the Coso Geothermal Area and also a prominent low shear velocity anomaly within the top 2 km, no significant anomaly below about 14 km depth, and a weakly resolved low velocity anomaly between 6 and 12 km depth. The anomaly in the top 2 km is believed to result from geothermal alteration in the shallow subsurface. No magmatic body is imaged

beneath 14 km depth, but the shear velocity anomaly between 6 and 12 km may be due to partial melt associated with a magma body. The amplitude of the inferred Vs anomaly for this body is dependent on its vertical thickness and the extent of vertical damping in the inversion. For this reason, the amplitude of this anomaly is ill-determined. This anomaly may be representative of magmatic processes that have altered the crustal structure through much of eastern California.

Acknowledgements:

The authors thank Dr. Wei-Chuang Huang for valuable conversations. Data used in this study result from a PASSCAL experiment performed from November 1998 to May 2000 and from the Southern California Seismic Network. Facilities of the IRIS Data Management System, and specifically the IRIS Data Management Center, were used to access the waveform and metadata required in this study. The IRIS DMS is funded by the National Science Foundation and specifically the GEO Directorate through the Instrumentation and Facilities Program of the National Science Foundationunder Cooperative Agreement EAR-0552316. This study was supported by the Navy Geothermal Program Office (GPO) under contract N68936-08-C-0061.

References

Armstrong, R. L., and P. Ward (1991), Evolving geographic patterns of Cenozoic magmatism in the North American Cordillera: The temporal and spatial association of magmatism and metamorphic core complexes, *Journal of Geophysical Research*, *96* (B8), 13,201-213,224.

Barmin, M. P., M. H. Ritzwoller & A. L. Levshin (2001), A fast and reliable method for surface wave tomography. *Pure and Appl. Geophy.s,* 158**,** 1351-1375.

Bartow, J. A. (1984), Geologic map and cross sections of the southeastern margin of the San Joaquin Valley, California, *U. S. Geological Survey Miscellaneous Investigations Series Map*, I-1496, scale 1:125,000, 2 sheets.

Bensen, G.D., M.H. Ritzwoller, M.P. Barmin, A.L. Levshin, F. Lin, M.P. Moschetti, N.M. Shapiro, and Y. Yang (2007), Processing seismic ambient noise data to obtain reliable broad-band surface wave dispersion measurements, *Geophys. J. Int.*, 169, 1239-1260, doi: 10.1111/j.1365-246X.2007.03374.x.

Bensen, G. D., M. H. Ritzwoller & N. M. Shapiro (2008), Broadband ambient noise surface wave tomography across the United States. *J. Geophys. Res., 113*, B05306, doi:10.1029/2007JB005248.

Bensen, G. D., M. H. Ritzwoller & Y. Yang (2009), A 3-D shear velocity model of the crust and uppermost mantle beneath the United States from ambient seismic noise. *Geophysical Journal International,* 177**,** 1177-1196.

Bhattacharyya, J., and J.M. Lees (2002), Seismicity and seismic stress in the Coso Range,Coso geothermal field, and Indian Wells Valley region, southeast-central California**.***Geol. Soc. Am.,* Memoir, 195, 243.

Bhattacharyya, J., S. Gross, J. Lees, and M. Hastings (1999), Recent earthquake sequences at Coso: Evidence for conjugate faulting and stress loading near a geothermal field**,** *Bull. Seism. Soc. Am.*; 89(3): 785 – 795.

Blakely, R. J., R. C. Jachens, J. P. Calzia, and V. E. Langenheim (1999), Cenozoic basins of the Death Valley extended terrain as reflected in regional-scale gravity anomalies, *in* L.A. Wright and B. W. Troxel (eds.), Cenozoic Basins of the Death Valley Region: Boulder, Colo., Geol. Soc. Amer. Spec. Paper 333, p. 1-16.

Campillo, M and A. Paul (2003), long-range correlations in the diffuse seismic coda, *Science* 24 vol. 299. 547- 549.

Cho, K. H., R. B. Herrmann, C. J. Ammon & K. Lee (2007), Imaging the upper crust of the Korean Peninsula by surface-wave tomography. *Bull. Seism. Soc. Am.,* 97**,** 198-207.

Combs, J. (1980), Heat Flow in the Coso Geothermal Area, Inyo County, California, *J. Geophys. Res.,* 85, no. B5, p. 2411-2424.

Crafford, A. E. J. (2007), Geologic map of Nevada, *U.S. Geol. Surv. Data Series*, 249, 1:250,000, v. 1.1 (2008).

de Voogd, B. L. Serpa, L. Brown, E. Hauser, S. Kaufman, J. Oliver, B. W. Troxel, J. Willemin[5] and L.A. Wright (1986), Death Valley bright spot: A midcrustal magma body in the southern Great Basin, California?, *Geology*, 14(1), 64-67.

Duffield, W. A., C. R. Bacon, and G. B. Dalrymple (1980), Late Cenozoic volcanism, geochronology, and structure of the Coso Range, Inyo County, California: *J. Geophys. Res.*, v. 85, p. 2381-2404.

Feng, Q., and J. M. Lees (1998), Microseismicity, stress, and fracture in the Coso geothermal field, California, *Tectonophy.s*, 289, 1-3, 221-238.

Hauksson, E. and J. Unruh (2007). Regional tectonics of the Coso geothermal area along the intracontinental plate boundary in central eastern California: Three-dimensional V-p and V-p/V-s models, spatial-temporal seismicity patterns, and seismogenic deformation. *J. Geophys. Res.*, 112 (B6) doi 10.1029/2006JB004721, art. B06309.

Hough, S.E., J.M. Lees, and F. Monastero (1999), Attenuation and source properties at the Coso Geothermal Area, California.*Bull. Seism. Soc. Am.*, 89(6): 1606 – 1619.

Jennings, C. W., (compiler) (1977), Geologic map of California, *Calif. Div. Mines Geol. Geol. Data Map*, 2, 1:750,000.

Jones, C. H. (1987), Is extension in Death Valley accommodated by thinning of the mantle lithosphere beneath the Sierra Nevada, California?. *Tectonics*, 6 (4) pp. 449-473.

Jones, C. H., and R. A. Phinney (1998), Seismic structure of the lithosphere from teleseismic converted arrivals observed at small arrays in the southern Sierra Nevada and vicinity, California, *Journal of Geophysical Research*, *103* (B5), 10,065-010,090.

Lees, J.M., and H. Wu (1999), *P* wave anisotropy, stress, and crack distribution at Coso Geothermal field, *J. Geophys. Res.,* 104, 17,955-17,974.

Lees, J.M., and H. Wu (2000), Poisson's ratio and porosity at Coso geothermal field, *J. Volcanol. Geotherm. Res.,* 157-173.

Lees, J.M. (2001), Three-dimensional anatomy of a geothermal field, Coso, south-east-central California, *Mem. Geol. Soc. Am.*, 195.

Lin, F. C., M. H. Ritzwoller, J. Townend, S. Bannister & M. K. Savage (2007), Ambient noise Rayleigh wave tomography of New Zealand. *Geophy. J. Int.,* 170**,** 649-666.

Lin, F. C., M. P. Moschetti & M. H. Ritzwoller (2008), Surface wave tomography of the western United States from ambient seismic noise: Rayleigh and Love wave phase velocity maps. *Geophy. J. Int.,,* 173**,** 281-298.

Lin, F.C., M.H. Ritzwoller, Y. Yang, M.P. Moschetti, and M.J. Fouch (2010), The stratification of seismic azimuthal anisotropy in the western US, *Nature Geoscience*, submitted.

Manley, C. R., and C. R. Bacon (2000), Rhyolite thermobarometry and the shallowing of the magma reservoir, Coso volcanic field, *California, J. Petrol.,* 41, 149 – 174.

McQuarrie, N., and M. Oskin (2010), Palinspastic restoration of NAVDat and implications for the origin of magmatism in southwestern North America, *J. Geophys. Res.*, doi: 10.1029/2009JB006435, in press.

Monastero, F.C., A. Katzenstein, J. Miller, J. R. Unruh, M. Adams, and K. Richards-Dinger (2005), The Coso geothermal field: A nascent metamorphic core complex. *Geol. Soc. Am. Bull.*, 117 (11) pp. 1534-1553.

Moschetti, M. P., M. H. Ritzwoller & N. M. Shapiro (2007), Surface wave tomography of the western United States from ambient seismic noise: Rayleigh wave group velocity maps. *Geochem. Geophys. Geosyst.*, *8*, Q08010, doi:10.1029/2007GC001655.

Moschetti, M.P., M.H. Ritzwoller, and F.C. Lin (2010a), Seismic evidence for widespread crustal deformation caused by extension in the western USA, *Nature*, **464**, N7290, 885-889.

Moschetti, M.P., M.H. Ritzwoller, F.C. Lin, and Y. Yang (2010b), Crustal shear velocity structure of the western US inferred from ambient noise and earthquake data, *J. Geophys. Res.*, in press.

Newman, G.A., E. Gasperikova, G. M. Hoversten, and P. E. Wannamaker (2008), Three-dimensional magnetotelluric characterization of the Coso geothermal field. *Geothermics*, 37 (4) pp. 369-399.

Nishida, K., H. Kawakatsu & K. Obara (2008), Three-dimensional crustal S wave velocity structure in Japan using microseismic data recorded by Hi-net tiltmeters. *J. Geophys. Res.*, *113*, B10302, doi:10.1029/2007JB005395.

Park, S. K., and B. Wernicke (2003), Electrical conductivity images of Quaternary faults and Tertiary detachments in the California Basin and Range, *Tectonics, 22* (4), DOI: 10.1029/2001TC001324, -.

Pluhar, C., R. S. Coe, J. C. Lewis, F. C. Monastero, and J. Glen (2006), Fault block kinematics at a releasing stepover of the Eastern California shear zone: Partitioning of rotation style in and around the Coso geothermal area and nascent metamorphic core complex. *Earth Planetary Science Letter,* 250 (1-2) pp. 134-163.

Pullammanappallil, S. K. and J. N. Louie (1993), Inversion of seismic reflection travel times using a nonlinear optimization scheme. *Geophysics*, 58 (11) pp. 1607-1620.

Pullammanappalil, S., B. Honjas, J. Unruh, and F. Monastero (2001), Use of advance data processing techniques in the imaging of the Coso geothermal field, Proceedings of the 26th Workshop on Geothermal Reservoir Engineering, Stanford University, Stanford, California, January 29-31.

Sabra, K.G., P. Gerstoft, P. Roux, W.A. Kuperman, and M.C. Fehler (2005), Surface wave tomography from microseism in southern California, *Geophys. Res. Lett.*, 32, L14311, doi:10.1029/2005GL023155.

Saito, M., (1988), DISPER80: A subroutine package for the calculation of seismic normal-mode solution, in *Seismological Algorithms*, edited by D.J. Doornbos, 293-319, Elsevier, New York.

Saltus, R. W., and A. H. Lachenbruch (1991), Thermal evolution of the Sierra Nevada: Tectonic implications of new heat flow data, *Tectonics*, *10* (2), 325-344.

Sanders, C., P. Ho-Liu, D. Rinn, and H. Kanamori, (1988) Anomalous Shear-Wave Attenuation in the Shallow Crust Beneath the Coso Volcanic Region, California, *J. Geophys. Res.-Solid Earth*, *93* (B4), 3321-3338.

Saygin, E. & B. L. N. Kennett (2010), Ambient seismic noise tomography of Australian continent. *Tectonophysics,* 481**,** 116-125.

Shapiro, N.M. M. Campillo, L. Stehly, and M.H. Ritzwoller (2005), High resolution surface wave tomography from ambient seismic noise, *Science*, 307(5715), 1615-1618, 11 March.

Taylor, T.R., J. F. Dewey, and F. C. Monastero (2008), Transtensional deformation of the brittle crust: Field observations and theoretical applications in the Coso-China lake region, Eastern margin of the Sierra Nevada microplate, southeastern California. *International Geology Review*, 50 (3) pp. 218-244.

Tsai, V. C., and M. P. Moschetti (2010). An explicit relationship between time-domain noise correlation and spatial autocorrelation (SPAC) results, *Geophys. J. Int.,* 182, 454-460, doi:10.1111/j.1365-246X.2010.04633.x.

Unruh, J.R., F. C. Monastero, and S. K. Pullammanappallil, (2008), The nascent Coso metamorphic core complex, east-central California: Brittle upper plate structure revealed by reflection seismic data. *International Geology Review,* 50 (3), 245-269.

Villaseñor, A., Y. Yang, M. H. Ritzwoller & J. Gallart (2007), Ambient noise surface wave tomography of the Iberian Peninsula: Implications for shallow seismic structure. *Geophys. Res. Lett.*, *34*, L11304, doi:10.1029/2007GL030164.

Walck, M.C., and R. W. Clayton (1987), *P* wave velocity variations in the Coso region, California, derived from local earthquake travel times, *J. Geophys, Res.*, 92, 393-405.

Walck, M.C. (1988), Three-dimensional *Vp/Vs* for the Coso region, California*, J. Geophys, Res.*, 93, 2047-2052.

Wernicke, B. (1985), Uniform-sense normal simple shear of the continental lithosphere, *Canadian Journal of Earth Sciences*, *22*, 108-125.

Wilson, C. K., C. H. Jones, and H. J. Gilbert (2003), A single-chamber silicic magma system inferred from shear-wave discontinuities of the crust and uppermost mantle, Coso geothermal area, California, *J. Geophys. Res.*, 108 [B5], 10.1029/2002JB001798.

Wu, H., and J.M. Lees (1996), Attenuation structure of Coso geothermal area, California, from wave pulse widths. *Bull. of the Seism. Soc. of America*; 86(5); 1574-1590.

Wu, H., and J.M. Lees (1999), Three-dimensional P and S velocity structures of the Coso geothermal area, California, from microseismic travel-time data, *J. Geophys, Res.*, 104, 13,217-13233.

Yang, Y. J., A. B. Li & M. H. Ritzwoller (2008a), Crustal and uppermost mantle structure in southern Africa revealed from ambient noise and teleseismic tomography. *Geophys. J. Int.,* 174**,** 235-248.

Yang, Y. J., M. H. Ritzwoller, F. C. Lin, M. P. Moschetti & N. M. Shapiro (2008b), Structure of the crust and uppermost mantle beneath the western United States revealed by ambient noise and earthquake tomography. *J. Geophys. Res., 113*, B12310, doi:10.1029/2008JB005833.

Yang, Y., M. Ritzwoller, A. Levshin & N. Shapiro (2007) Ambient noise rayleigh wave tomography across Europe. *Geophys. J. Int,* 168**,** 259-274.

Yang, Y., et al., Rayleigh wave phase velocity maps of Tibet and the surrounding regions from ambient seismic noise tomography (2010), *Geochem., Geophys., Geosys.*, **11** (8), Q08010, doi:10.1029/2010GC003119.

Yao, H.J. , van der Hilst, R.D., de Hoop (2006), M.V. Surface-wave array tomography in SE Tibet from ambient seismic noise and two-station analysis - I. Phase velocity maps. *Geophys. J. Int.,* 1**66** (2), 732-744.

Young, C. and R.W. Ward (1980), Three-dimensional Q^{-1} model of the Coso Hot Springs known geothermal resource, *J. Geophys. Res.* ,85(B5).

Zheng, S. H., X. L. Sun, X. D. Song, Y. J. Yang & M. H. Ritzwoller (2008), Surface wave tomography of China from ambient seismic noise correlation. *Geochem. Geophys. Geosyst.*, *9*, Q05020, doi:10.1029/2008GC001981.

Figure Captions:

Figure 1. (a) Distribution of seismic stations in the Coso Geothermal Area and surrounding areas used in this study. There are 67 Southern California Seismic Network (SCSN) stations denoted by the red and white triangles with continuous data being archived by the Southern California Earthquake Data Center (SCEDC) since January 2008. The two white triangles show the locations of a broadband station CLC and a short-period station WRC. The blue triangles denote the Coso PASSCAL stations. Black lines denote faults. (b) Place names mentioned in text: CB: Cantil Basin; CR: Coso Range; IM: Inyo Mountains; IWV: Indian Wells Valley; LI: Lake Isabella; MS: Maricopa sub-basin; OL: Owens Lake.

Figure 2. Examples of amplitude spectra between 0.1 and 1 Hz for daily ambient noise data from five stations: MPM, LBTE1, LBTE5, WHAE1 and WHA0 from top to bottom. Station MPM is from the SCSN network, the other four are PASSCAL stations. Stations MPM and WHA0 are broadband stations whereas stations LBTE1, LBTE5 and WHAE1 are short-period stations.

Figure 3. (a) Examples of daily time-series for five stations from the Coso PASSCAL experiment. Time-series for short-period stations LBTE1, LBTE3 and LBTN1 display a series of glitches whereas broadband stations LBTE5 and LBTN5 do not. (b) Band-pass filtering

time-series from 0.1 to 1 Hz (1-10 sec period) reduces glitches compared to those in Fig. 3a. (c) Applying running-absolute-mean normalization to time series shown in Fig. 3b suppresses glitches further.

Figure 4. One-month cross-correlations from June 1999 among the Coso PASSCAL stations from periods of (a) 1 to 3 sec (b) and 3 to 10 sec, respectively. The inclined dashed lines indicate the 3.0 km/s move-out. Clear surface wave signals appear in the cross-correlations from 3 to 10 sec period (Fig. 4b) but not from 1 to 3 sec.

Figure 5. One-month cross-correlations for June 2008 filtered between periods of 3 and 10 sec for (a) broadband station CLC and other stations and (b) short-period station WRC and other stations. Clear Rayleigh waves at 3-10 sec period appear for both broadband and short-period stations with a propagation of about 3 km/sec, as delineated by the two inclined dashed lines. Locations of stations CLC and WRC are indicated in Fig. 1.

Figure 6. (a) Ray paths between stations CGO and LRL (red) and between stations CWC and THE (blue). The red star marks the location of the Coso Geothermal Area. (b) The measured Rayleigh wave phase speed dispersion curves based on the symmetric components; the red curve is for station pair CGO-LRL and the blue curve for CWC-TEH. Phase velocities of the path CGO-LRL path (red lines) through the Coso Geothermal Area are depressed compared with the path between stations CWC-the that transits the Sierra Nevada Mountains.

Figure 7. Path coverage and resolution at periods of 4 and 9 sec for Rayleigh wave phase speed tomography on a 0.25° x 0.25° grid.

Figure 8. Phase velocity maps at periods of 3, 5,7 and 9 sec. Velocity perturbations relative to the averages across each map are plotted in the region encompassing the stations, as outlined by the polygons. Two gray contours indicate resolution of 50 and 200 km are plotted on each phase velocity map.

Figure 9. (a) Location of two points in the Sierra Nevada (blue star) and near the Coso Geothermal Area (red star) to illustrate inversion results. (b) Rayleigh wave phase velocity dispersion curves from the dispersion maps (circles) for the two locations shown in Fig. 9a. The solid lines are the dispersion curves produced by the Vs model estimated by linearized inversion, shown in (c). Red lines and symbols are for the Coso point and blue lines and symbols are for the Sierra Nevada.

Figure 10. Maps of Rayleigh wave shear velocity at depths of 1, 3, 6, 10, 14 and 18 km are plotted as perturbations to averages at each depth: 1 km (2.867 km/s), 3 km (3.174 km/s), 6 km (3.319 km/s), 10 km (3.452 km/s), 14 km (3.524 km/s), 18 km (3.574 km/s). Two gray contours of resolution at resolution scales of 50 and 200 km from the 5 sec phase velocity map (Fig. 8b) are plotted in each map. The three dash lines in Fig. 9a delineate the surface locations of the three vertical transects shown in Fig. 12.

Figure 11. Exposures of Cenozoic igneous rocks in eastern California (Jennings, 1977; Crafford, 2007) compared with outline (black) of low Vs (<~3% at 6 km depth, Fig. 10c). Extent of inverted region delineated by gray outline.

Figure 12. Vertical cross-sections of shear velocities plotted as both absolute values (left) and perturbations relative to the 1D Vs averages (right). The locations of the cross-sections are shown in Fig. 10a. Abbreviations: COSO: the Coso Geothermal Area; SN: the Sierra Nevada Mountains; DV: Death Valley; MD: the Mojave Desert; GV: California's Great Valley; GF: the Garlock Fault.

Figure 13. Comparison of Rayleigh wave phase velocity curves from four different vertical profiles: background model containing no low velocity zones (black), 10% low velocity anomaly in the top 4 km (red), 10% low velocity anomaly between depths of 6 and 10 km depth (pink), and 10% low velocity anomaly between 10 and 15 km depth (blue). (a) Plots of the velocity profiles for the four models. (b) The associated dispersion curves.

Figure 14. Resolution tests for three input Vs models with low velocity anomalies at different depths. At left are the input models with low velocity bodies at 0-6 km, 4-10 km, and 8-16 km depth and at right are the recovered models.

Figure 15. Effect of changing vertical smoothing on inversions for the Vs structure directly beneath the Coso Geothermal Area. (a) Resulting models from three different vertical smoothing schemes; blue: strongly smoothed as in our inversions shown in Figs. 10, 12, and 14 (same as Fig. 9c); red: less strongly smoothed; black dashed: even less vertical smoothing (b) The dispersion data from 3 sec to 10 sec period near the Coso Geothermal Area (red circles, same as Fig. 9b) and the resulting dispersion curves from each differently smoothed inversion, similarly colored. Strong vertical smoothing reveals a very weak low velocity zone from 6 to 8 km depth. Reducing smoothing produces a stronger low velocity anomaly between depths of 6 and 12 km and increasingly higher velocities below 15 km depth.

Table 1: The numbers of selected paths for tomography at different periods

Period (sec)	Number of paths
3.00	310
3.50	362
4.00	454
4.50	490
5.00	491
6.00	590
7.00	571
8.00	459
9.00	365
10.00	288

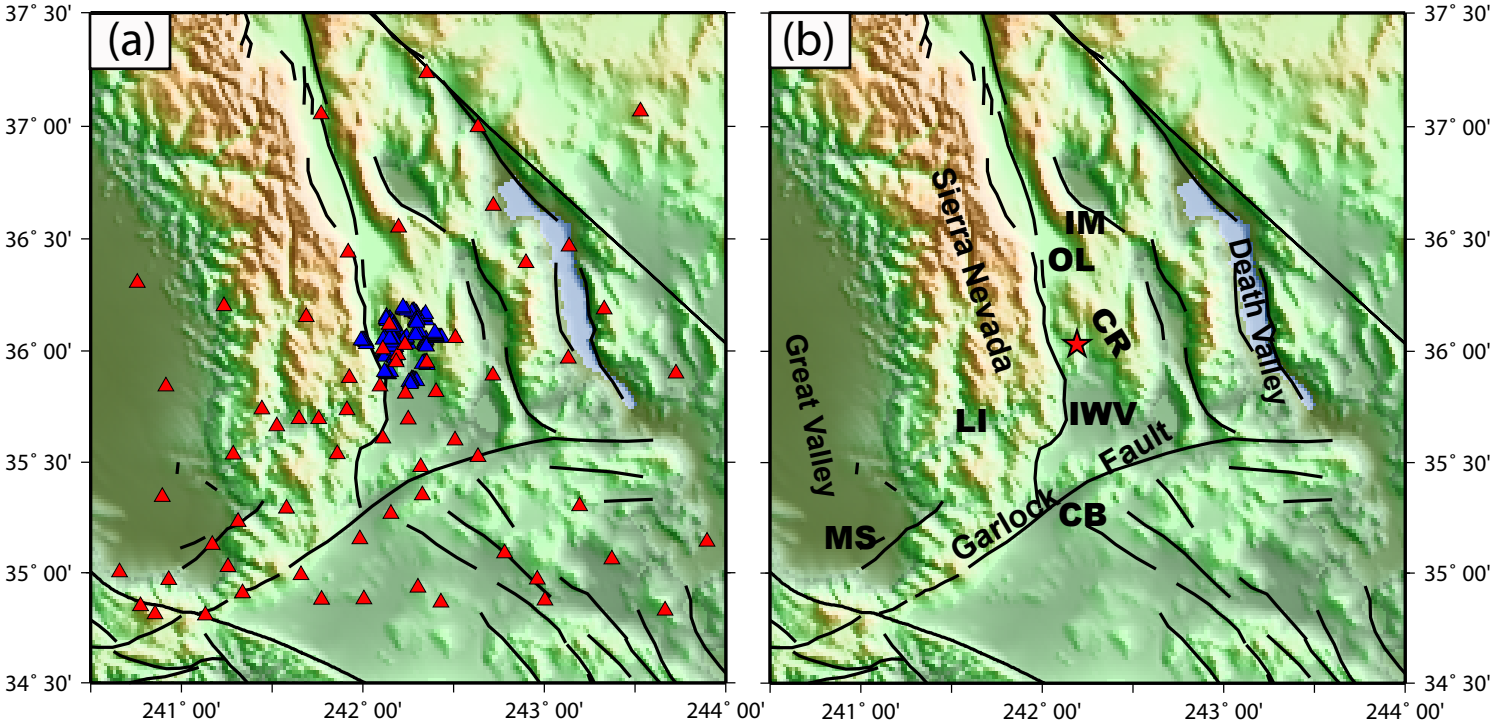
(a)
(b)
37° 30'
37° 00'
36° 30'
36° 00'
35° 30'
35° 00'
34° 30'
241° 00'
242° 00'
243° 00'
244° 00'
Sierra Nevada
Great Valley
Death Valley
Garlock Fault
IM
OL
CR
LI
IWV
CB
MS

Figure1

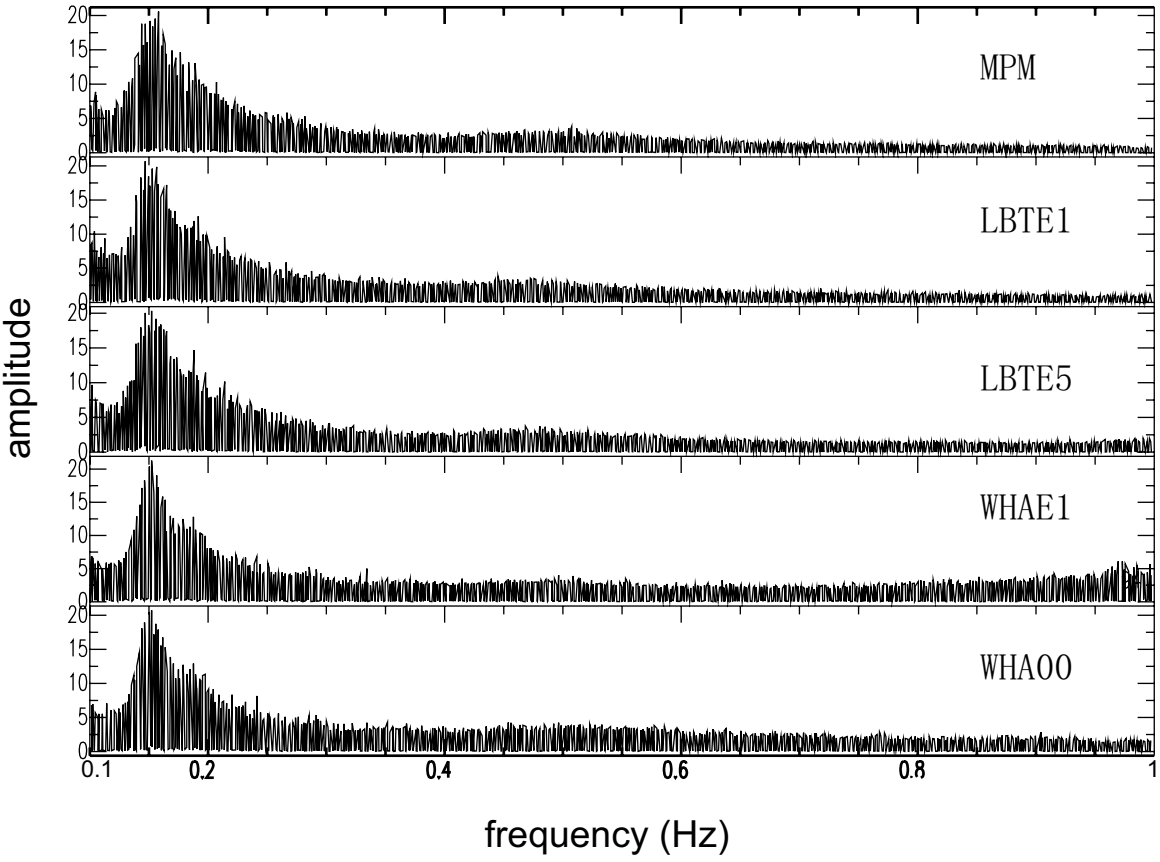
amplitude
MPM
LBTE1
LBTE5
WHAE1
WHA00
0.1
0.2
0.4
0.6
0.8
1
frequency (Hz)

Figure2

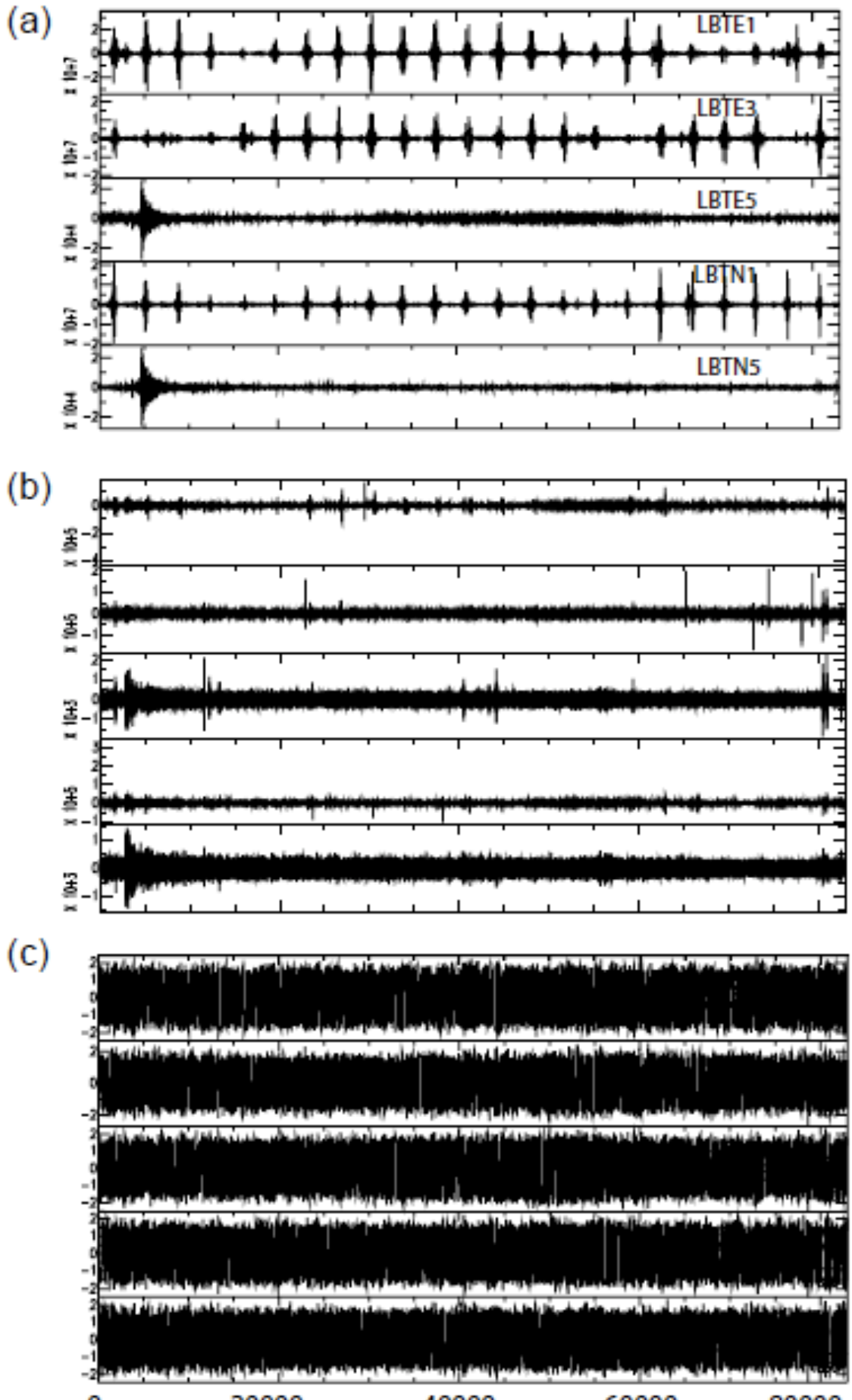
(a)
LBTE1
LBTE3
LBTE5
LBTN1
LBTN5
(b)
(c)
0
20000
40000
60000
80000
Time (sec)

Figure 3

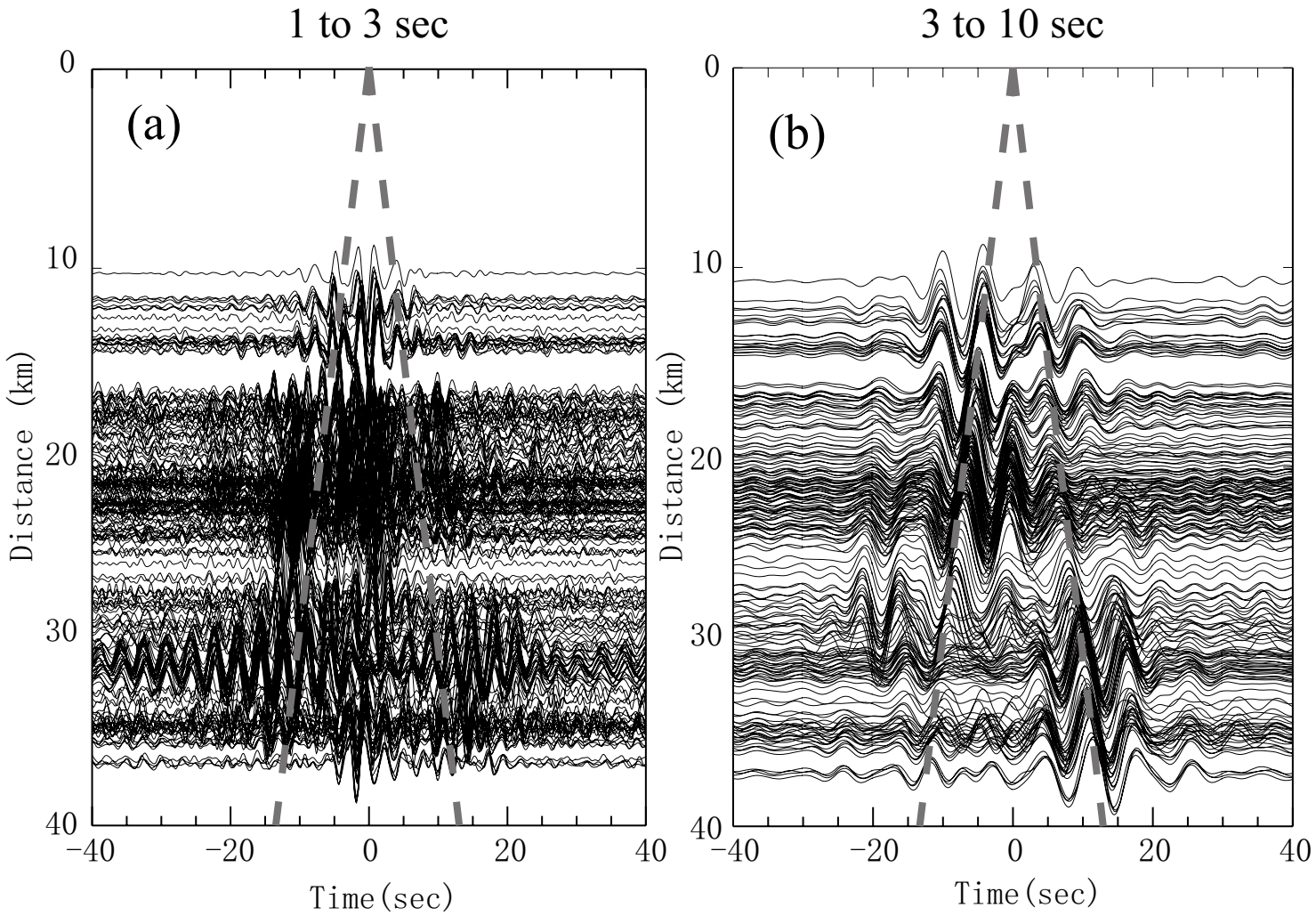
1 to 3 sec
3 to 10 sec
(a)
(b)
Distance (km)
Time(sec)
0
10
20
30
40
-40
-20
0
20
40

Figure4

(a) cross-correlations between station CLC and other stations

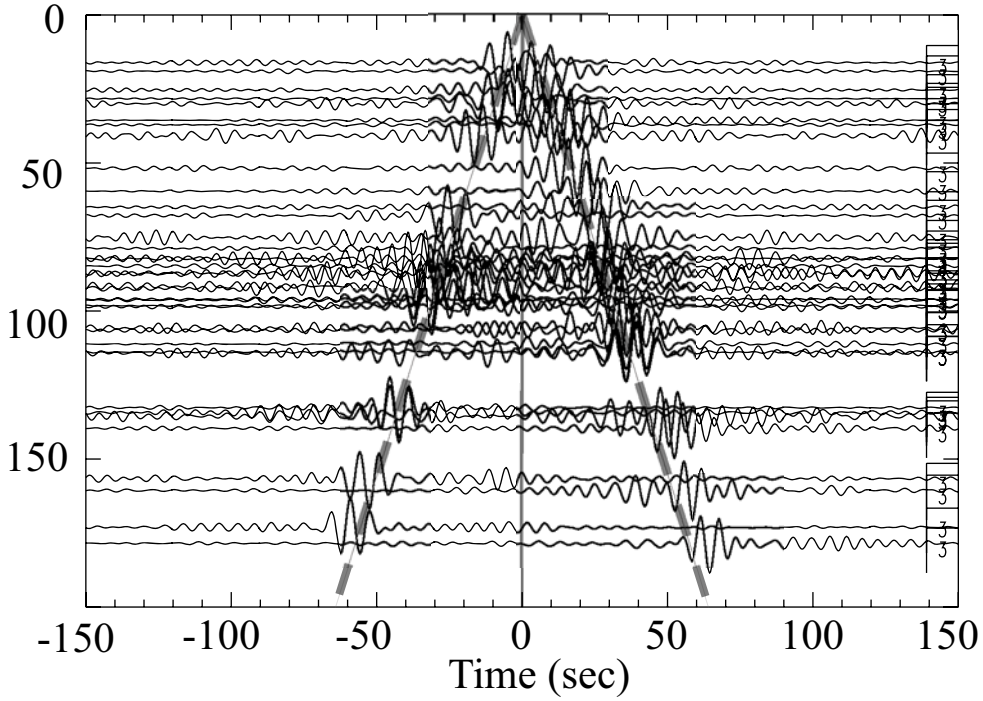

(b) cross-correlations between station WRC and other stations

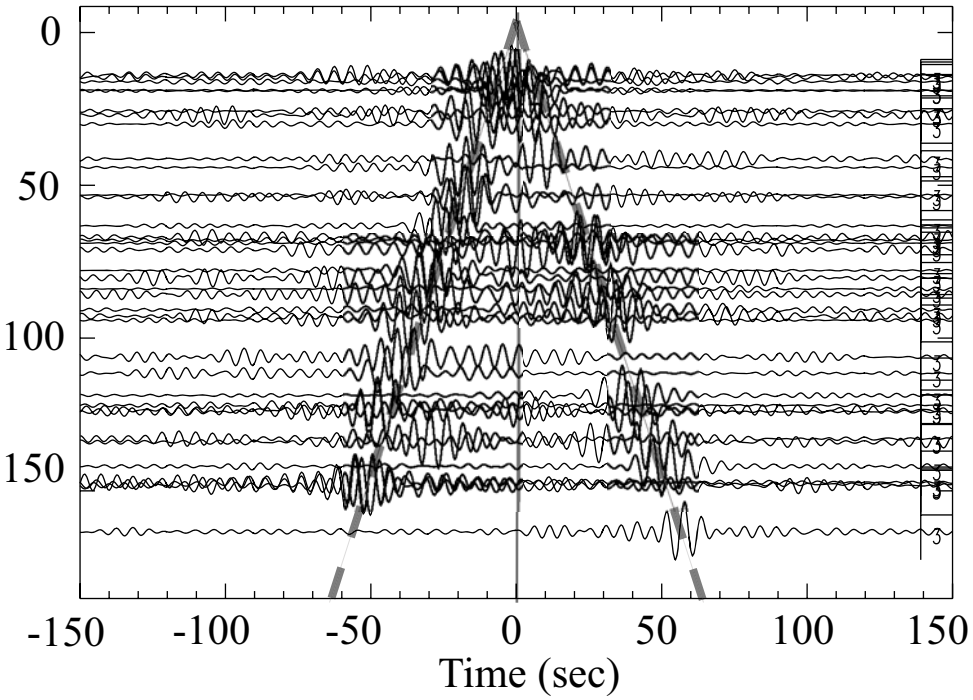

Figure5

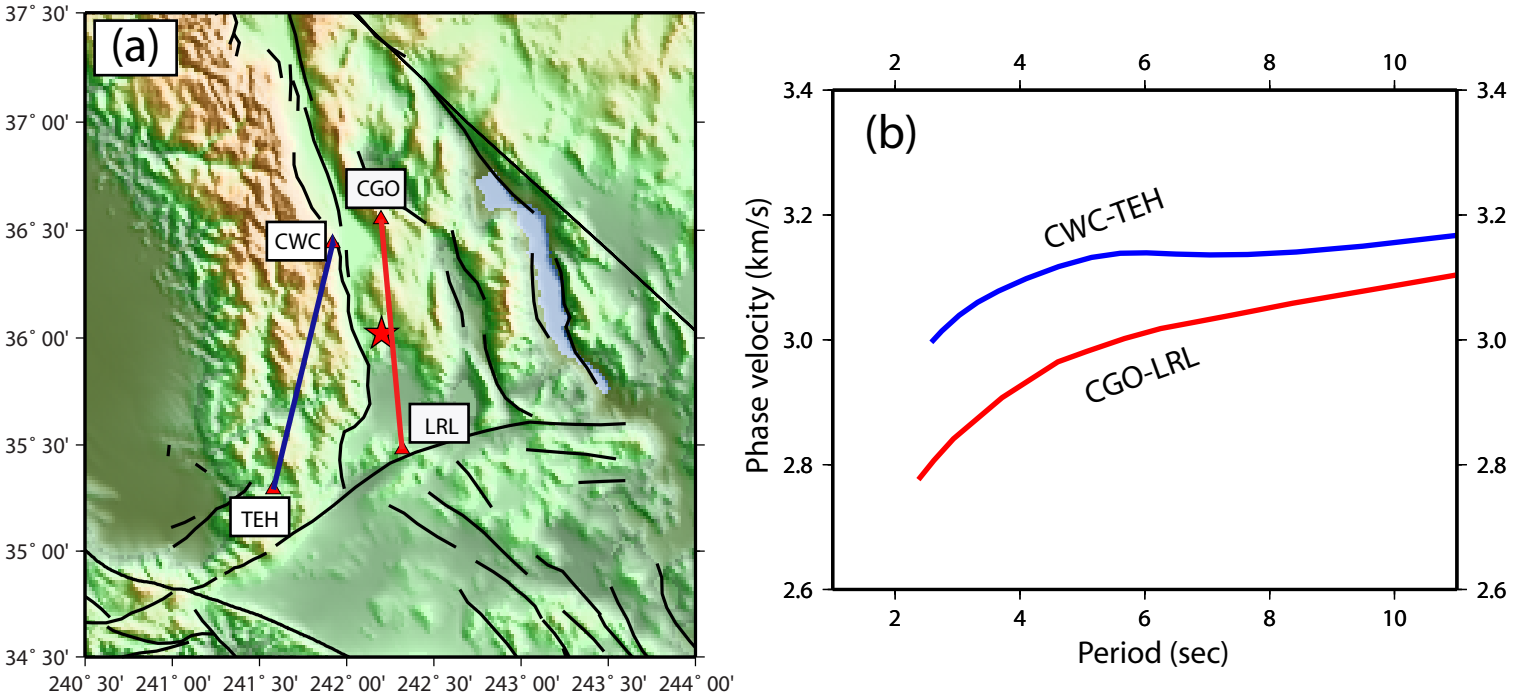
(a)
CGO
CWC
LRL
TEH
37° 30'
37° 00'
36° 30'
36° 00'
35° 30'
35° 00'
34° 30'
240° 30'
241° 00'
241° 30'
242° 00'
242° 30'
243° 00'
243° 30'
244° 00'
(b)
CWC-TEH
CGO-LRL
Phase velocity (km/s)
Period (sec)
2
4
6
8
10
2.6
2.8
3.0
3.2
3.4

Figure 6

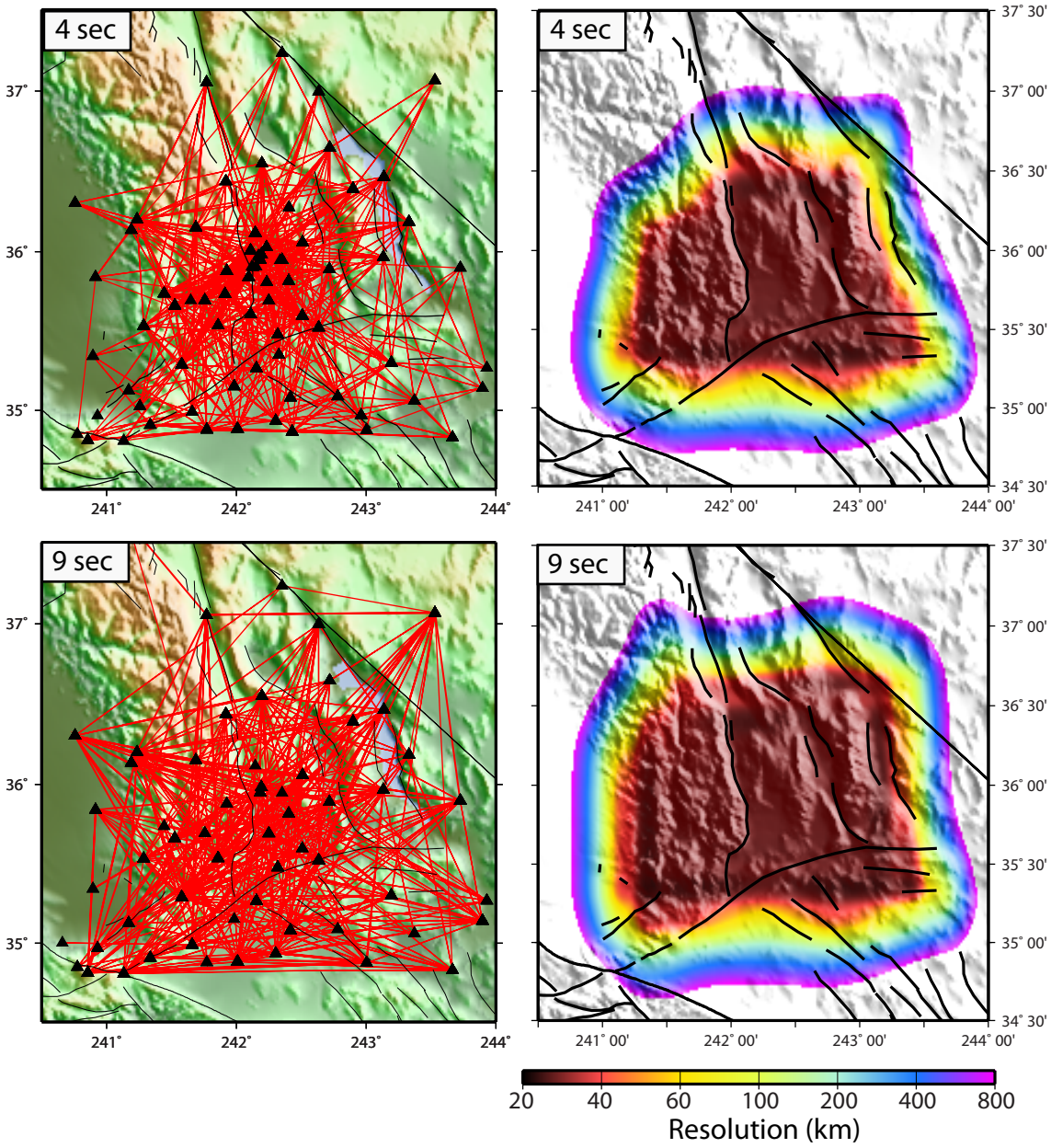
4 sec
4 sec
9 sec
9 sec
37°
36°
35°
241°
242°
243°
244°
37° 30'
37° 00'
36° 30'
36° 00'
35° 30'
35° 00'
34° 30'
241° 00'
242° 00'
243° 00'
244° 00'
20
40
60
100
200
400
800
Resolution (km)

Figure 7

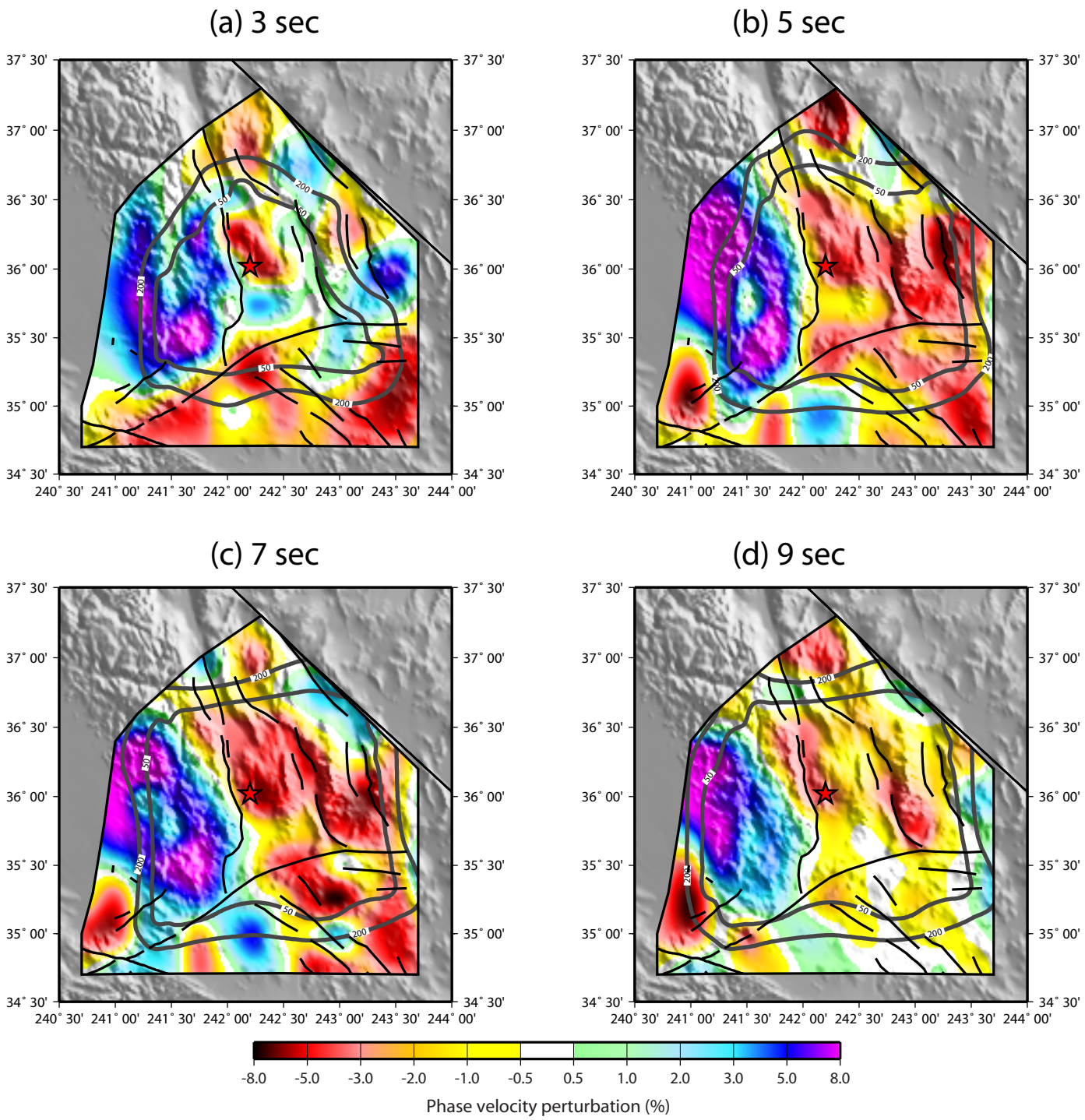
(a) 3 sec
(b) 5 sec
(c) 7 sec
(d) 9 sec
37° 30'
37° 00'
36° 30'
36° 00'
35° 30'
35° 00'
34° 30'
240° 30'
241° 00'
241° 30'
242° 00'
242° 30'
243° 00'
243° 30'
244° 00'
50
200
-8.0
-5.0
-3.0
-2.0
-1.0
-0.5
0.5
1.0
2.0
3.0
5.0
8.0
Phase velocity perturbation (%)

Figure8

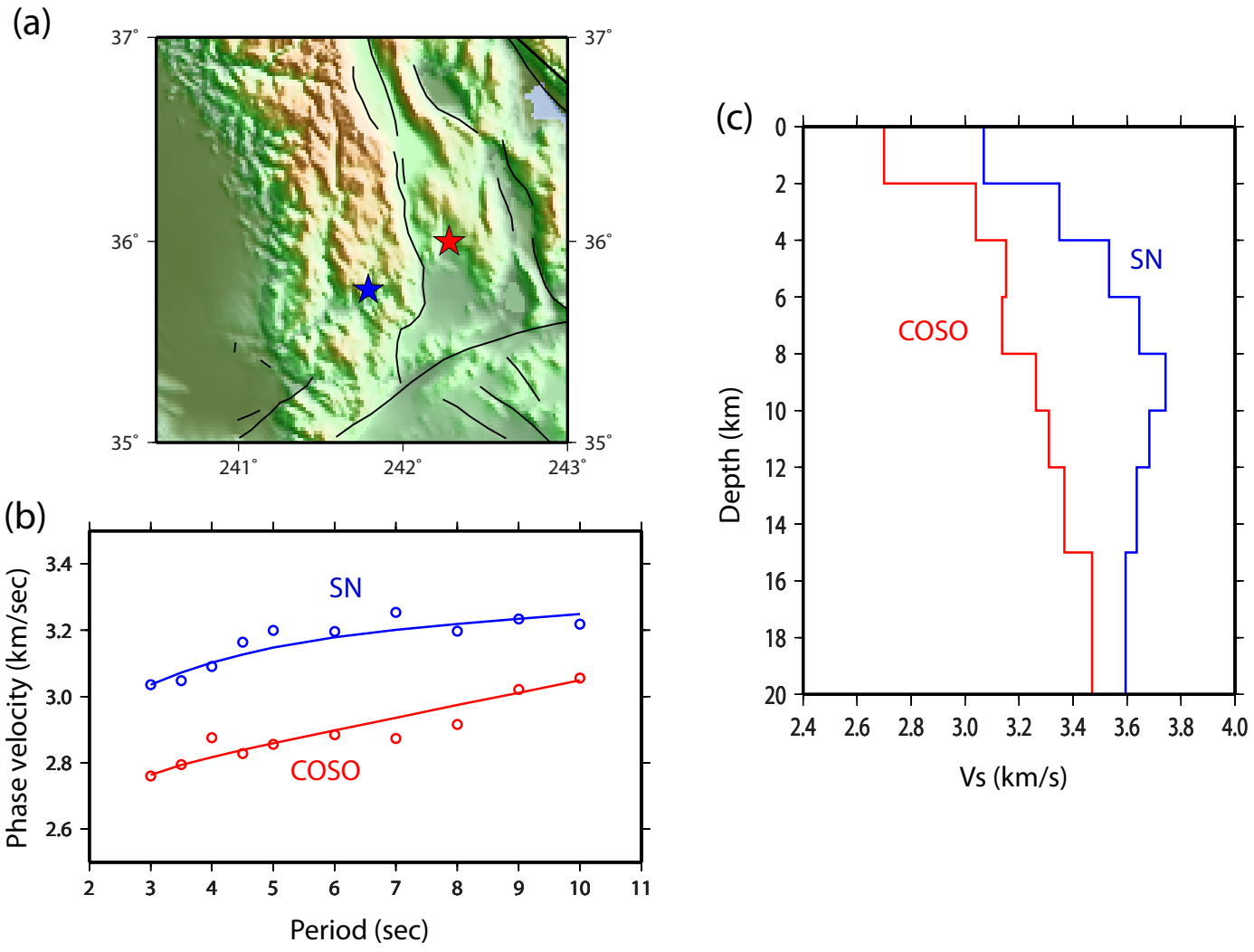
(a)
37°
36°
35°
241°
242°
243°
(b)
Phase velocity (km/sec)
Period (sec)
SN
COSO
(c)
Depth (km)
Vs (km/s)
SN
COSO

Figure 9

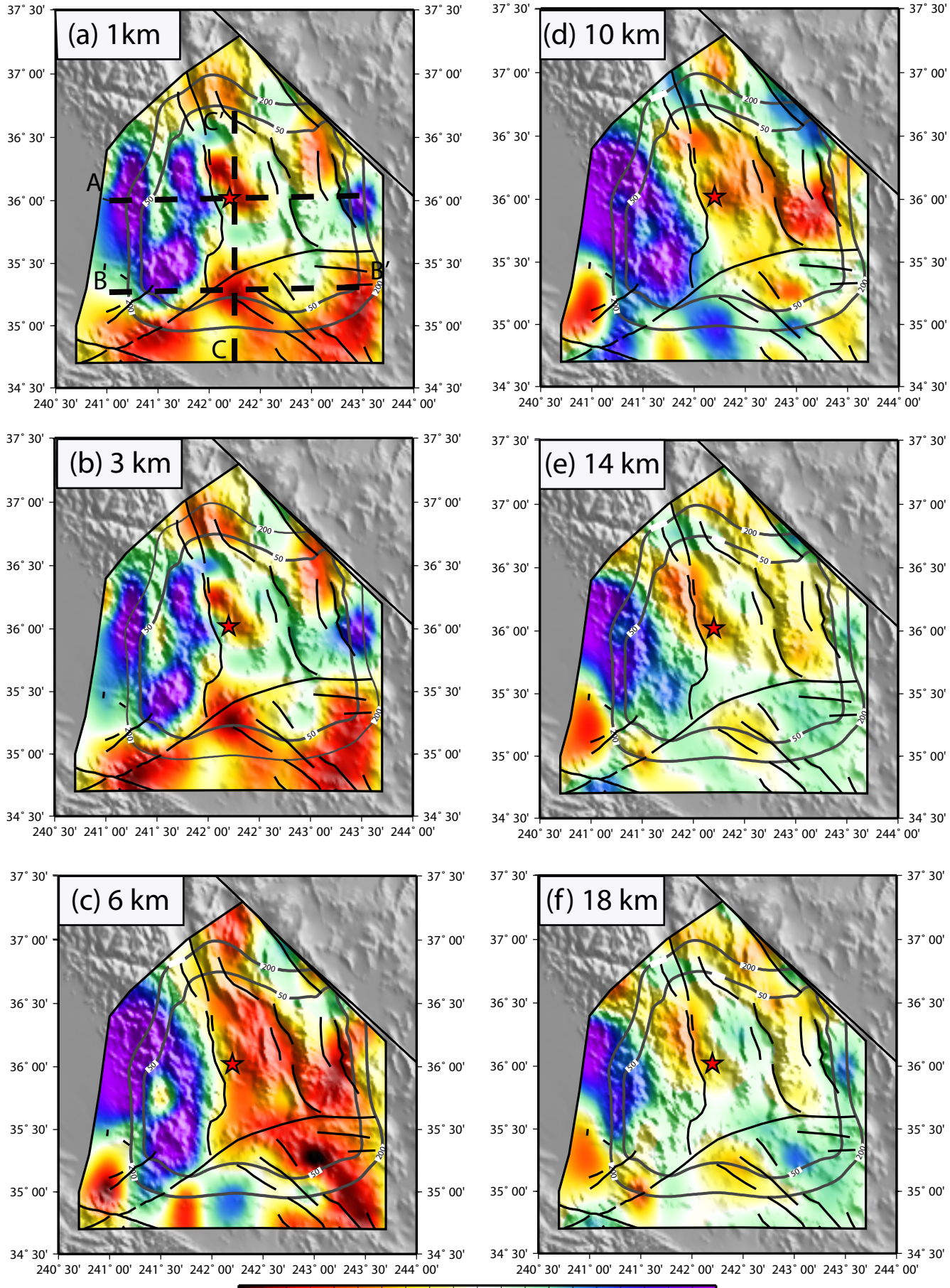
(a) 1km
(b) 3 km
(c) 6 km
(d) 10 km
(e) 14 km
(f) 18 km
A
A′
B
B′
C
C′
37° 30'
37° 00'
36° 30'
36° 00'
35° 30'
35° 00'
34° 30'
240° 30'
241° 00'
241° 30'
242° 00'
242° 30'
243° 00'
243° 30'
244° 00'
-10 -9 -8 -7 -6 -5 -4 -3 -2 -1 0 1 2 3 4 5 6 7 8 9 10
Vs perturbation (%)

Figure10

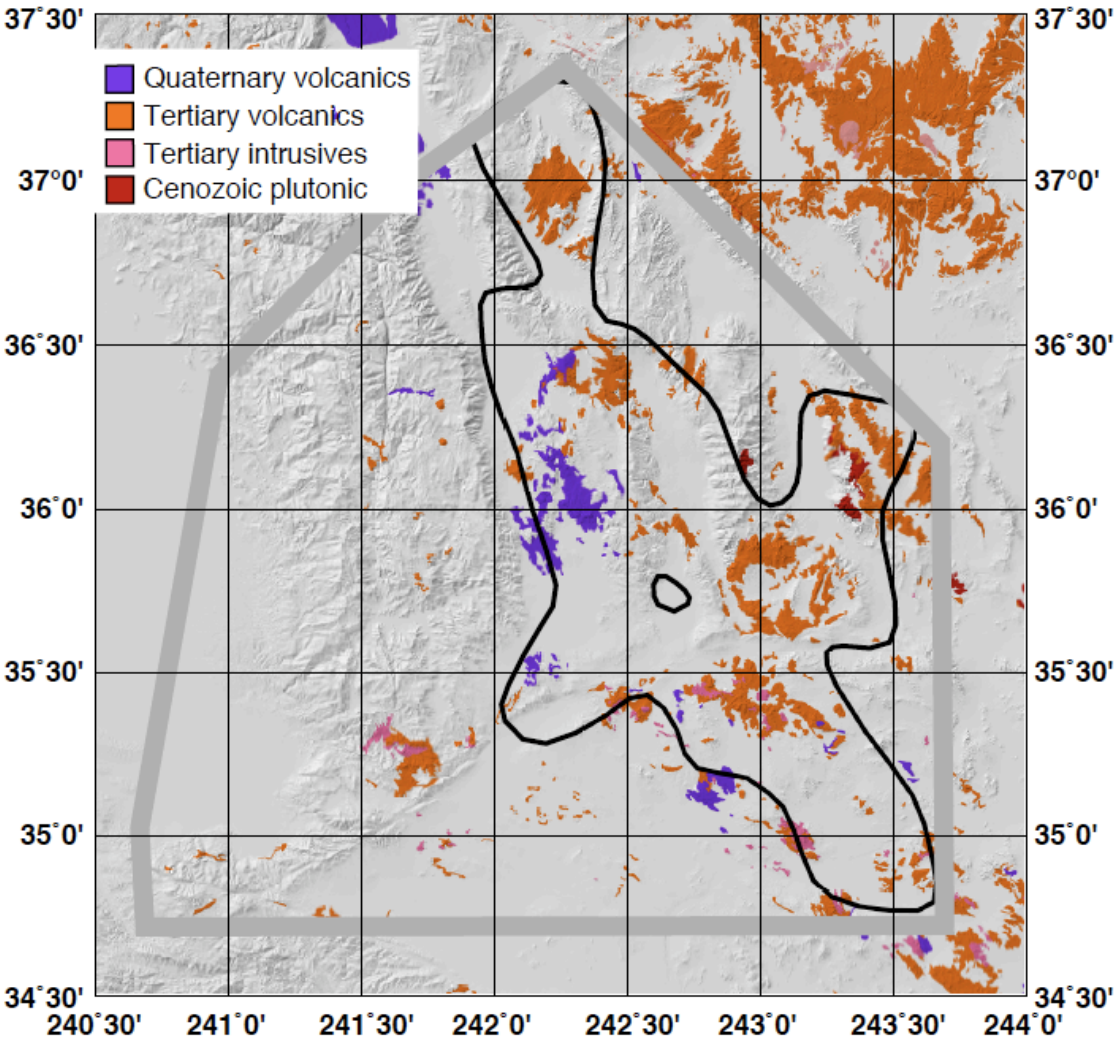
Quaternary volcanics
Tertiary volcanics
Tertiary intrusives
Cenozoic plutonic
37°30'
37°0'
36°30'
36°0'
35°30'
35°0'
34°30'
240°30'
241°0'
241°30'
242°0'
242°30'
243°0'
243°30'
244°0'

Figure 11

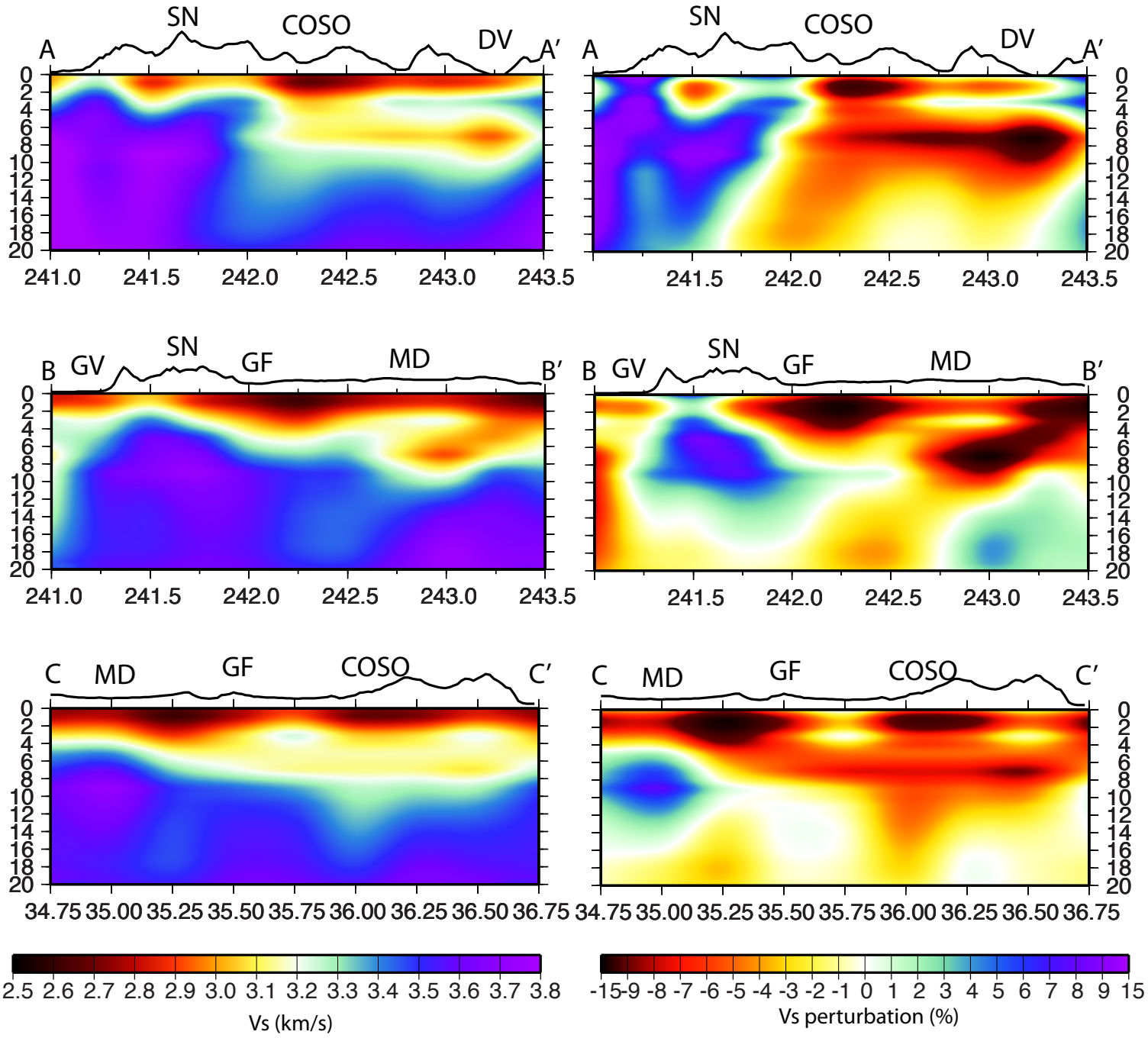
A
SN
COSO
DV
A′
B
GV
SN
GF
MD
B′
C
MD
GF
COSO
C′
0 2 4 6 8 10 12 14 16 18 20
241.0 241.5 242.0 242.5 243.0 243.5
34.75 35.00 35.25 35.50 35.75 36.00 36.25 36.50 36.75
2.5 2.6 2.7 2.8 2.9 3.0 3.1 3.2 3.3 3.4 3.5 3.6 3.7 3.8
Vs (km/s)
-15 -9 -8 -7 -6 -5 -4 -3 -2 -1 0 1 2 3 4 5 6 7 8 9 15
Vs perturbation (%)

Figure 12

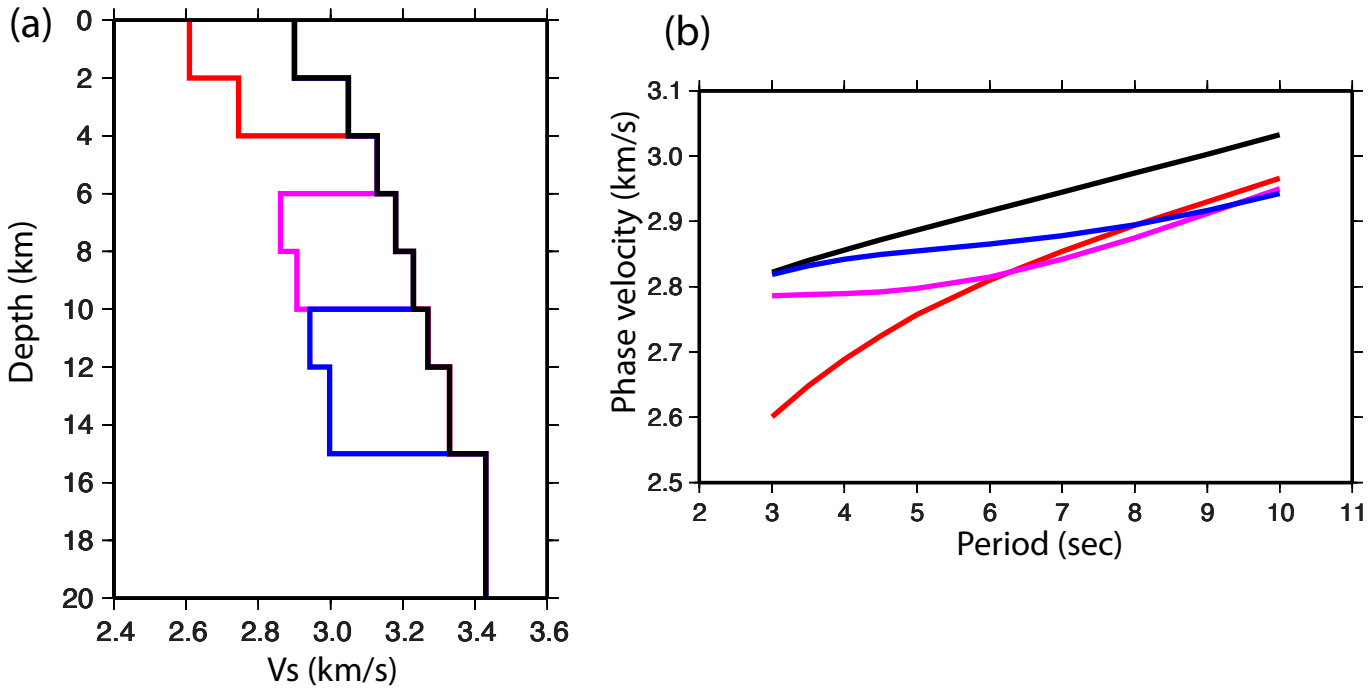
(a)
Depth (km)
0
2
4
6
8
10
12
14
16
18
20
2.4
2.6
2.8
3.0
3.2
3.4
3.6
Vs (km/s)
(b)
Phase velocity (km/s)
3.1
3.0
2.9
2.8
2.7
2.6
2.5
2
3
4
5
6
7
8
9
10
11
Period (sec)

Figure 13

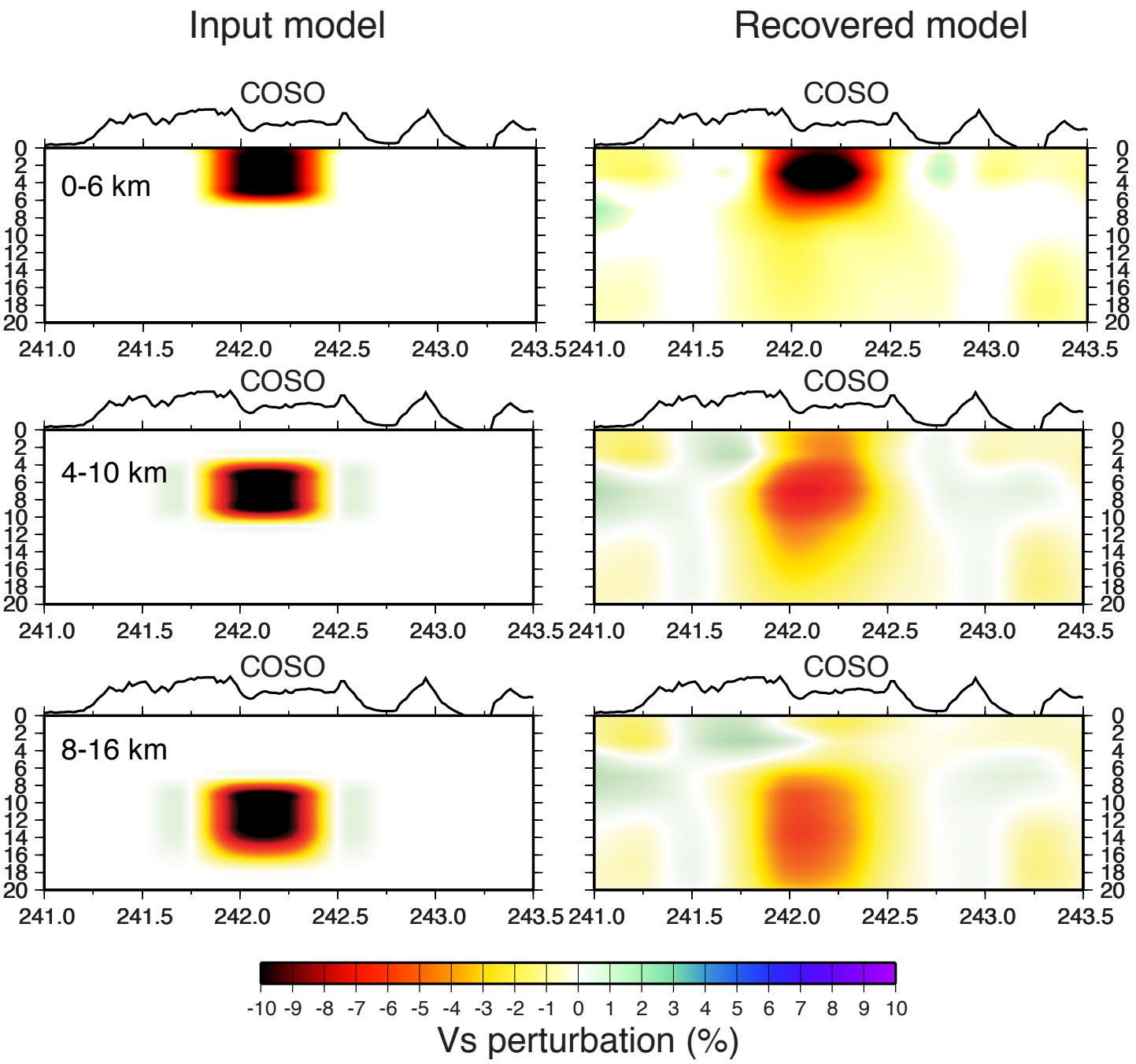
Input model
Recovered model
COSO
0-6 km
4-10 km
8-16 km
0 2 4 6 8 10 12 14 16 18 20
241.0 241.5 242.0 242.5 243.0 243.5
-10 -9 -8 -7 -6 -5 -4 -3 -2 -1 0 1 2 3 4 5 6 7 8 9 10
Vs perturbation (%)

Figure 14

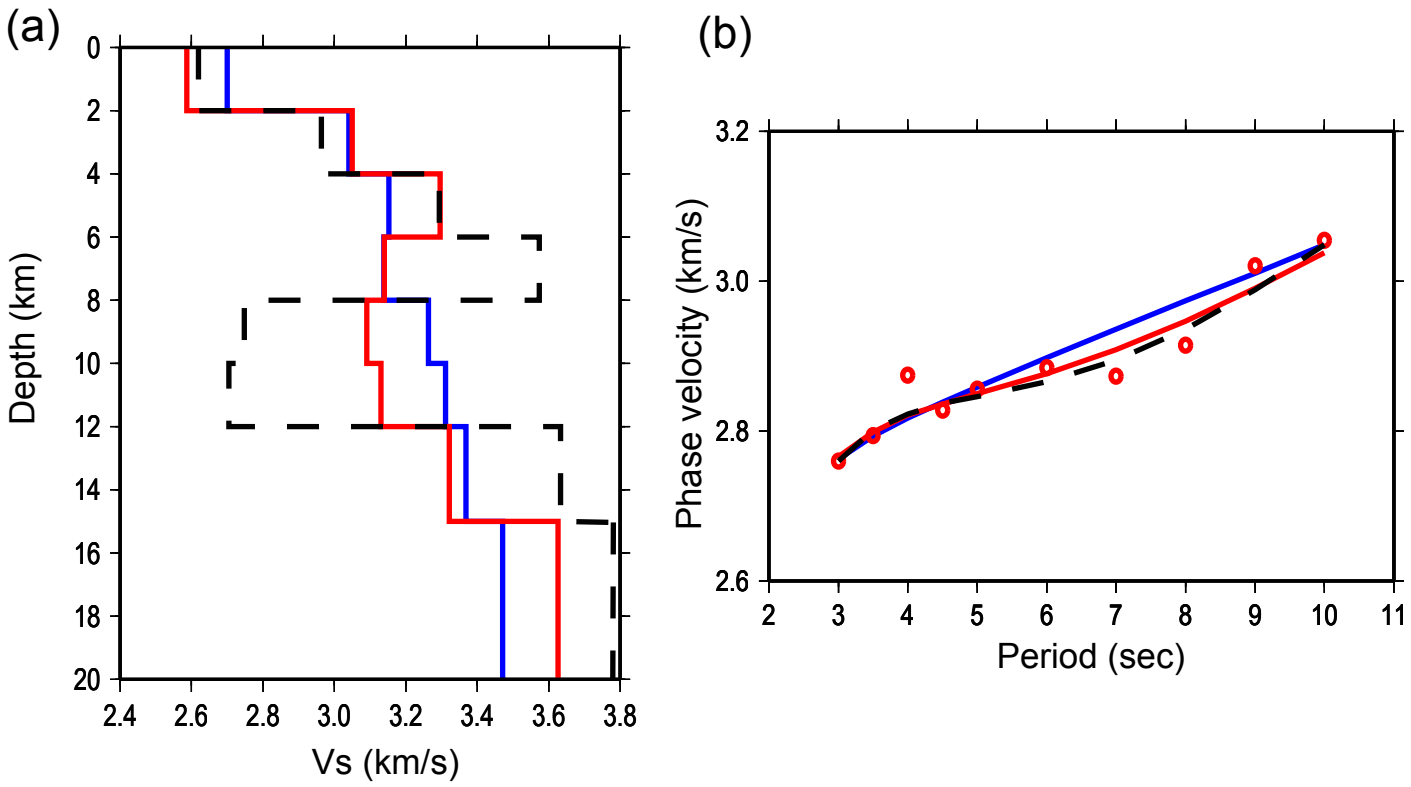
(a)
Depth (km)
0
2
4
6
8
10
12
14
16
18
20
2.4
2.6
2.8
3.0
3.2
3.4
3.6
3.8
Vs (km/s)
(b)
Phase velocity (km/s)
3.2
3.0
2.8
2.6
2
3
4
5
6
7
8
9
10
11
Period (sec)

Figure 15